

**Final Technical Report
for
ELF/VLF Electromagnetic
Detection and Characterization
of Deeply Buried Targets**

June 22, 1998

**Sponsored by
Defense Advanced Research Projects Agency (DOD)
(STO)**

ARPA Order No. D611, Amdt 27

**Issued by U.S. Army Aviation & Missile Command Under
Contract # DAAH01-97-C-R032**

Contractor

**CODAR Ocean Sensors, Ltd.
1000 Fremont Ave., Suite K
Los Altos, CA 94024**

Principal Investigator

**Dr. Donald E. Barrick
(650) 941-5897**

Effective Date of Contract

November 12, 1997

Short Title of Work

**ELF/VLF for Deeply Buried
Targets**

Contract Expiration Date

July 10, 1998

Reporting Period

Final

DISCLAIMER

The views and conclusions contained in this document are those of the authors and should not be interpreted as representing the official policies, either expressed or implied of the Defense Advanced Research Projects Agency or the U.S. Government.

Approved for public release; distribution unlimited

DTIC QUALITY INSPECTED 1

19980707 240

Table of Contents

Table of Contents.....	i
Abstract.....	ii
Introduction and Summary.....	1
Overview.....	1
Report Outline.....	2
Source Modeling.....	3
Remote Man-Made Sources.....	3
Local Sources.....	12
Natural Sources - External Noise.....	17
Underground Structure Modeling.....	18
Dipole Definitions and the Long Wavelength Approximation.....	18
NEC-3 Models.....	19
Ellipsoid Dipole Models.....	19
Perturbed Field Calculations.....	24
Total Field Calculation.....	26
Sensor Response Modeling.....	31
Suggested Phase II Tasks.....	40
References.....	41
Appendix A.....	

Abstract

In the light of the current and ongoing needs of DoD and other agencies for detection of subsurface structures and monitoring of activities within those structures there is a crucial need for tools that allow one to evaluate the myriad of proposed VLF/ELF sensor systems. The overall objective of this effort is to develop analytical tools to model and assess proposed ELF/VLF sensor systems for detection of underground structures. The approach taken is to a) model the primary electric and magnetic fields generated by local (e.g. current loops or electric dipoles), remote (e.g. HAARP/HIPAS), and natural sources (e.g. external noise); b) model the perturbed fields due to the specified underground structures; c) combine the primary and perturbed fields along with the external noise for an effective field at the sensor; d) model the sensor (the GEM-2 from Geophex, Ltd.) given the manufacturer's specifications and then using these results e) evaluate the response of the sensor system to the specified underground structure.

Introduction and Summary

Overview

This is the Final Report for the SBIR effort entitled "ELF/VLF Electromagnetic Detection and Characterization of Deeply Buried Targets" sponsored by the Defense Advanced Research Projects Agency. The overall objective of this effort is to develop analytical tools to model and assess proposed ELF/VLF sensor systems for detection of underground structures. The approach taken is to refine and extend existing tools to model:

- Primary fields generated by
 - Local Sources
 - Remote Sources
 - Natural Sources
- Perturbed fields due to underground structures
- Calculate the total field at the sensor location
- The response of the candidate sensor to the total fields - The sensor system selected is the GEM-2 manufactured by Geophex, Ltd.

This effort is of significance in light of the current and ongoing needs of DoD and other agencies for detection of subsurface structures and monitoring of activities within those structures. Given this need it is crucial to possess tools that allow one to evaluate the myriad of proposed VLF/ELF sensor systems:

- Claims are often supported by sparse technical analysis/tests
- Intercomparison among competing candidates is impossible
- Optimization is difficult and costly

The present effort is meant to provide MATLAB analysis tools to allow performance predictions by ourselves and the wider ELF/VLF community: DoD agencies, SETA contractors, instrument designers. The theoretical formulas are given in Appendix A. These formulas have been applied to a specific commercial sensor system, the Geophex GEM-2 and the results are presented. Also given is an outline of a Phase II SBIR effort to further validate and extend these tools.

Report Outline

The rest of this report is broken into six sections listed below:

- Source Modeling
 - Remote Man-Made Sources
 - Local Man-Made Sources
 - Natural Sources
- Structure Modeling
- Perturbed Field Calculations
- Total Field Calculations
- Sensor Response Modeling Results
- Suggested Phase II Tasks
- Appendix A: Sommerfeld Integral Results for a three-layer medium

Source Modeling

The ELF/VLF electromagnetic sources examined in this study are of three types

- Remote man-made sources, e.g. HAARP/HIPAS
- Local sources, e.g. metal-detector loop
- Natural sources, e.g. lighting

This section examines these three sources types and reviews the results of the effort so far under this program.

Remote Man-Made Sources

The High Power Auroral Stimulation Observatory (HIPAS) and the High Frequency Active Auroral Research Program (HAARP) are capable of exciting plasma structures in the ionosphere to act as elevated electric or magnetic dipoles. These dipoles can be then modulated at specified ELF/VLF frequencies to produce standing/traveling wave electromagnetic fields in the Earth-Ionosphere Cavity.

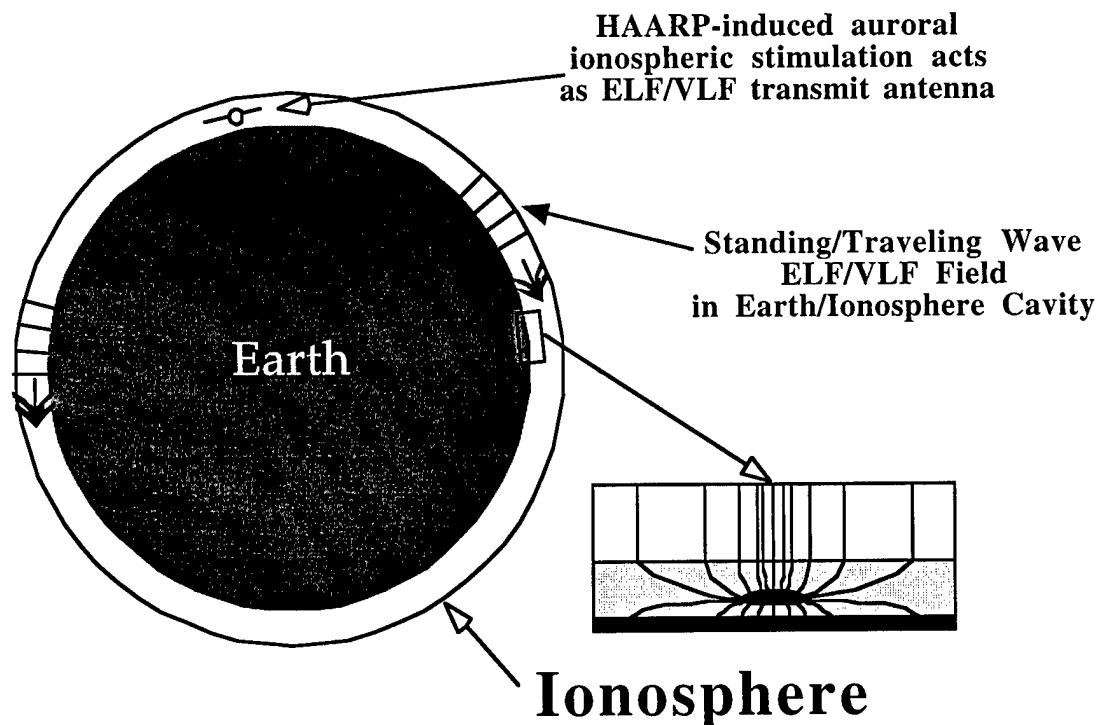


Figure 1: Earth-Ionosphere Cavity

As shown in Figure 1, these fields could then excite underground structures at some distance (thousands of kilometers) from the source. These perturbed fields would be measured by local sensors. This section deals just with the fields excited by these

remote man-made sources.

Perfectly Conducting Earth-Ionosphere Cavity

The Earth-Ionosphere Cavity has been studied by many researchers utilizing a variety of approximate mathematical techniques and any number of ionospheric models. Since this program is an effort designed to produce tools that will provide the user with validated results, we felt that a solid set of test cases built on exact solutions was required before developing more elaborate models. To this end we have examined the case of a perfectly conducting spherical cavity excited by the following four dipole sources (Barrick, 1998):

- Vertical Electric Dipole (VED)
- Horizontal Electric Dipole (HED)
- Vertical Magnetic Dipole (VMD)
- Horizontal Magnetic Dipole (HMD)

The form of the solution to the perfectly conducting spherical cavity for these sources is written in a straightforward way to yield **E/H** solutions of the form (assuming the dipole/loop is situated at a radius b above the "North Pole" of a spherical polar coordinate system) with the observation point at (r, θ, ϕ) :

$$\cos(m[\phi - \phi_0]) \sum_{n=0}^{\infty} a_n(b) \hat{F}_n(kr) P_n^m(\cos \theta)$$

where

- b - radius from center of Earth to location of the dipole/loop source
- $a_n(b)$ - coefficient determined by boundary conditions and dipole height
- m - 0 or 1 depending on field polarization and dipole orientation
- ϕ_0 - 0 or $\pi/2$ depending on field polarization and dipole orientation
- $\hat{F}_n(kr)$ - $\hat{J}_n(kr)$ or $\hat{H}_n(kr)$ depending on source height.

$$\hat{J}_n(kr) = \sqrt{\frac{\pi z}{2}} J_{n+1/2}(z) \text{ - Schelkunoff's spherical Bessel function}$$

$$\hat{H}_n(kr) = \sqrt{\frac{\pi z}{2}} H_{n+1/2}(z) \text{ - Schelkunoff's spherical Hankel function}$$

$$k \text{ - wave number of ELF/VLF source } \left(= \frac{2\pi}{\lambda} \right)$$

$$P_n^m(\cos \theta) \text{ - associated Legendre function}$$

The solutions for the four dipole sources have been obtained and programmed in MATLAB. An example of this is given below for the vertical **E** field and vertical **H**

field due to a VED.

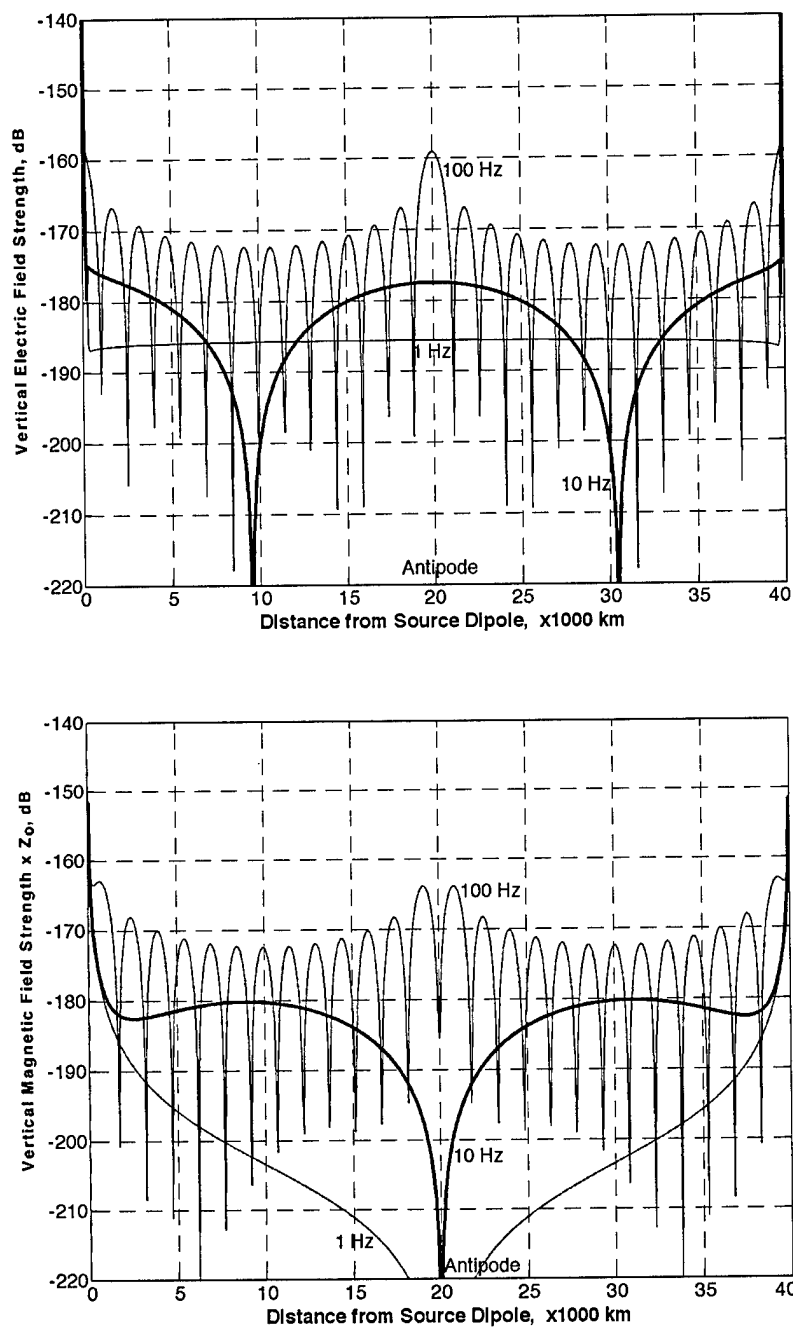


Figure 2: Fields for vertical electric dipole source in a perfectly conducting Earth-Ionosphere cavity ($Z_0 \approx 377 \Omega$)

As a check we compared these solutions with an approximate solution due to Wait based on the Watson-Transform (see below). The comparison is shown in Figure 3.

The agreement at 50 MHz is good except in the near zone (distance < 200 km). Agreement is not expected at 5 Hz because $kr < 1$ where Wait's approximation fails.

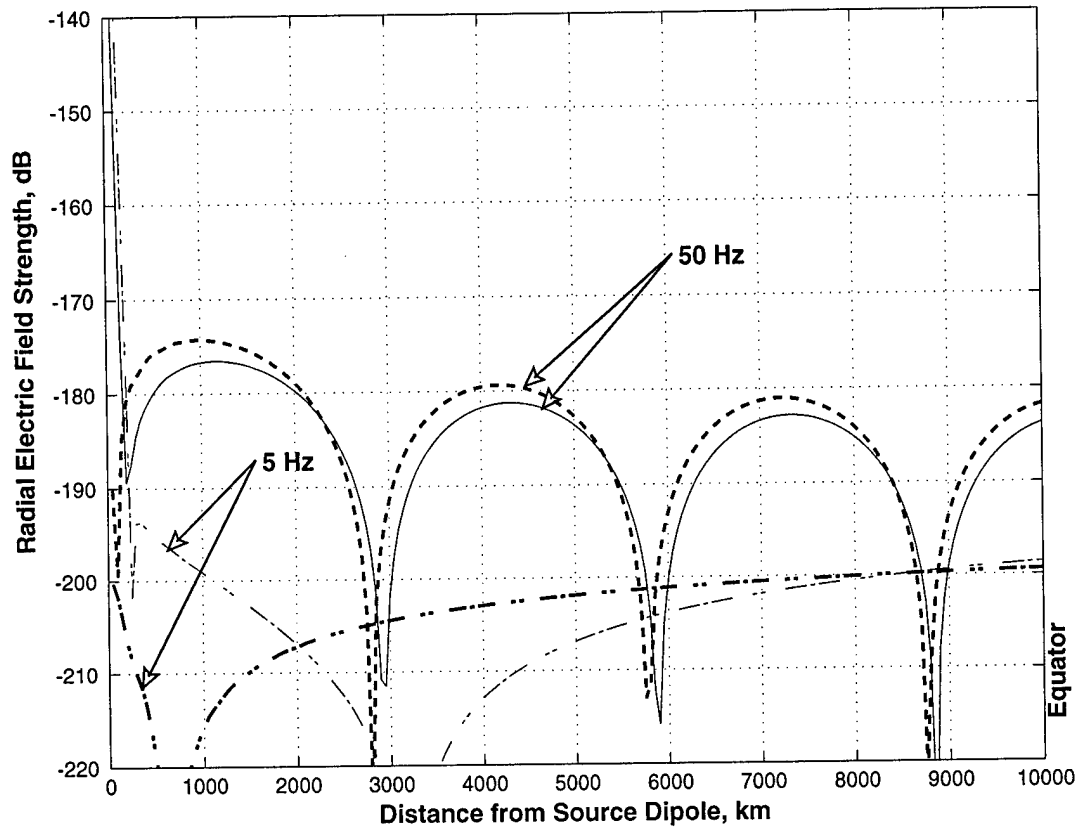


Figure 3: Comparison with asymptotic method of Wait (VED)
Heavy curves are from Wait, light curves are the exact solution

Watson-Transform Solutions

The exact form solution given above

$$\cos(m[\phi - \phi_0]) \sum_{n=0}^{\infty} a_n(b) \hat{F}_n(kr) P_n^m(\cos \theta)$$

can be transformed via analytic continuation (Watson Transform) to another exact solution (Wait, 1996, Chapter VI) with (roughly) the same form, but a different set of order indices

$$\cos(m[\phi - \phi_0]) \sum_{n=0}^{\infty} \gamma_n(b) \hat{F}_{v_n}(kr) P_{v_n}^m(\cos(\pi - \theta))$$

where the order values (subscripts) v_n take on complex values related to the modes of the Earth-Ionosphere cavity.

The Watson transform solutions are useful because at ELF and VLF frequencies only one term of the sum is required for ranges > 1000 km and only about 10 terms are

required as close in as 50 km. Typically these solutions have been studied and simplified for higher frequency regions (VLF and above) using asymptotic approximations to the Bessel and Legendre functions of complex order. The commercial package *Mathematica*[®] developed by Wolfram Research, Inc. allows direct and exact computation to any desired decimal precision of these functions for any complex order and complex argument. Using *Mathematica* we have compared the conventional solution with the Watson transformed solution for the perfectly conducting surface case. The solutions are identical. Using the Watson transform solution we have also included a lossy ionospheric impedance boundary. These comparisons are plotted in Figure 4. Note that the conventional solution and the Watson transformed solution overlie each other.

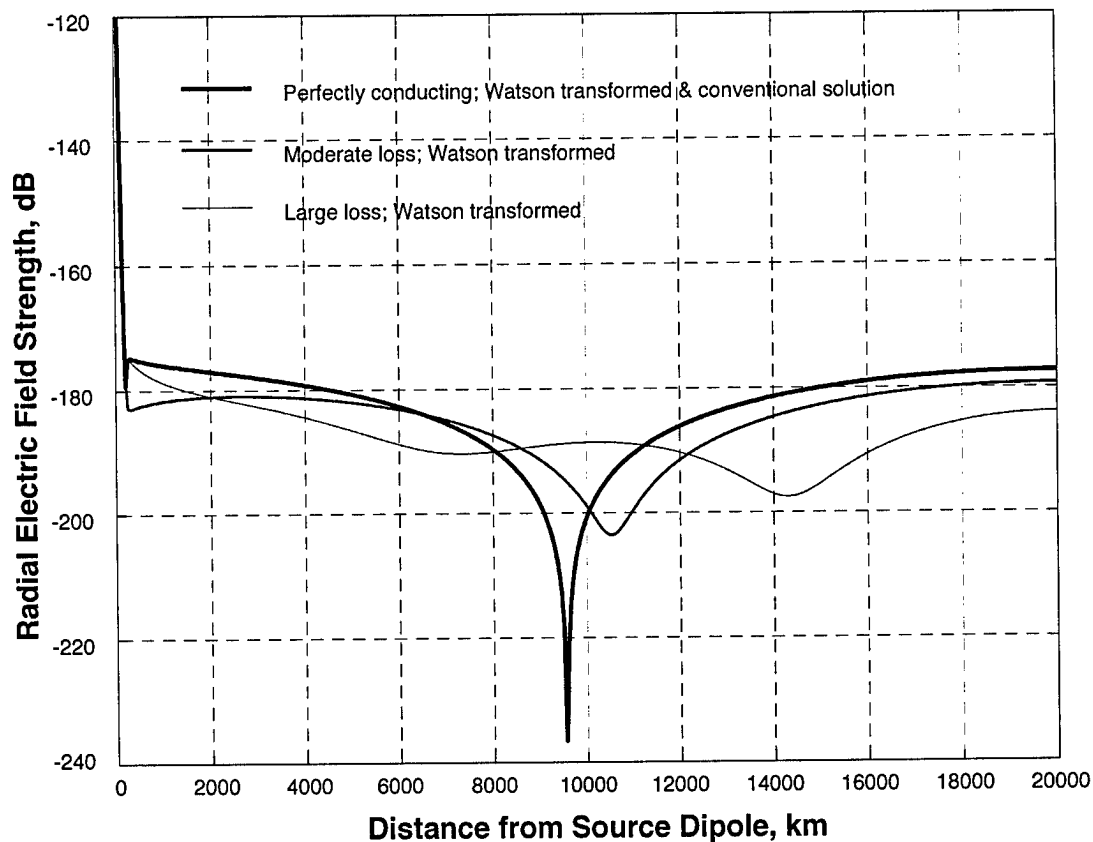


Figure 4: Comparison of Watson transform and conventional solution and the Watson transform solution for 2 lossy ionosphere cases - all at 10 Hz. The moderate loss relative impedance is $0.0028-i0.0027$; the large loss relative impedance is $0.029-i0.027$.

Ionospheric Modeling

In the discussion above, the fields were calculated based on a perfectly conducting or impedance boundary. At the Earth surface this is a good approximation for ELF and VLF, because of the high conductivity of earth and sea water. This approximation must be examined further for the ionospheric boundary. This is because a) the dielectric properties of the ionosphere gradually change from approximately free space values below the ionosphere to something approaching a perfect conductor and then back to free space values beyond the ionosphere and b) the free space wavelengths at ELF and VLF are of the order of hundreds to thousands of kilometers and so the ionosphere might appear to be a relatively thin, penetratable lossy dielectric layer. This section examines the validity of the impedance boundary layer approximation. Also examined is the proper value of the effective impedance and the effective height of the layer¹.

For the cases we are considering the dielectric properties of the ionosphere are determined by the electron density and the electron collision frequency. The various layers of the ionosphere (D, E, F,...) change as a function of time of day, season of year, sun spot cycle time and latitude/longitude.

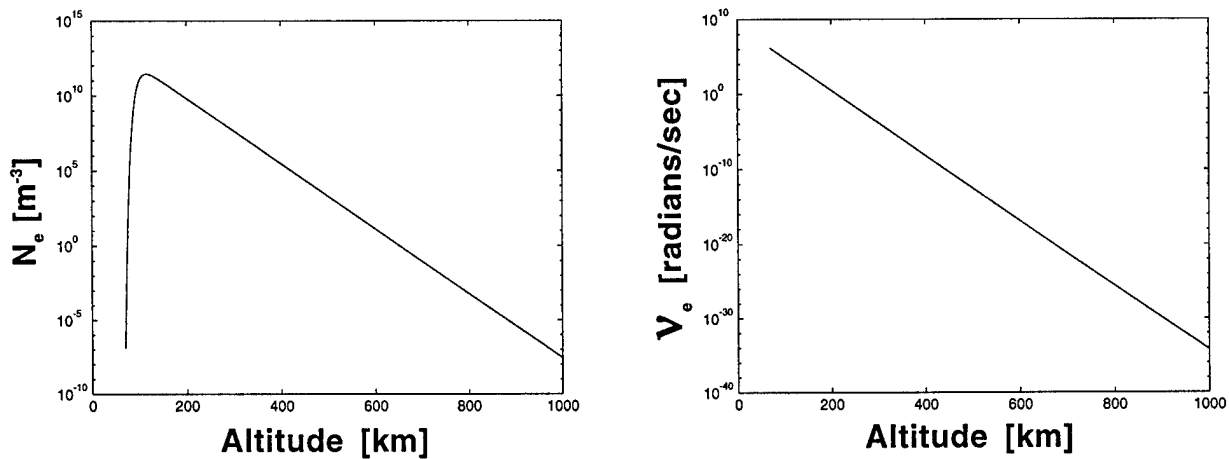


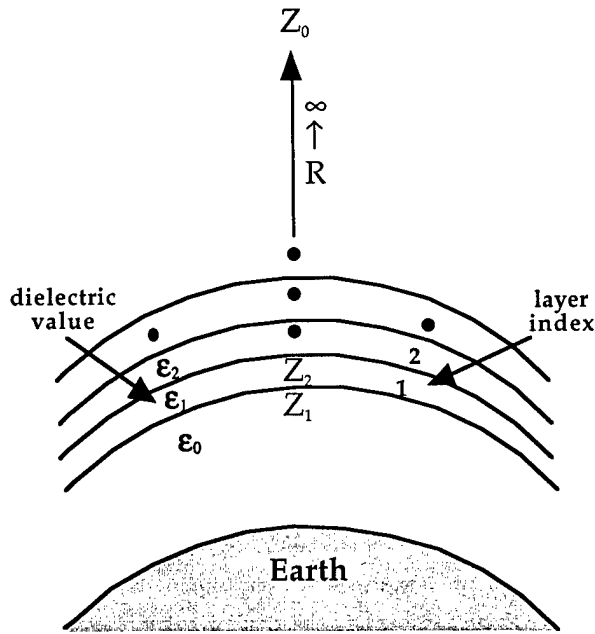
Figure 5: Electron density distribution and effective electron collision frequency for the ionospheric model used in this study.

A full description would include all of these layers and dependencies and such

¹ It should be noted that the Earth's magnetic field has a significant effect on the effective dielectric properties. This issue will not be examined during this phase of the effort. It should be addressed in future efforts, especially in examining HAARP/HIPAS measured data.

models are available (Budden, 1985; Davies, 1969). For the level of accuracy required for this study we will model the electron density as a single Chapman E-layer (Budden, 1985, pp 7-14). This electron density distribution is given in Figure 5 along with the effective electron collision frequency (Budden, 1985 p12).

The ionosphere can be modeled as a series of thin, concentric shells surrounding the



Ionosphere modeled as a series of layers with an effective impedance, Z_n , at each layer interface. As the distance above the Earth goes to infinity, the impedance goes to the free space value Z_0 ($\approx 377 \Omega$)

Figure 6: Layered ionosphere model

Earth, as seen in Figure 6. This model can be formulated in a number of ways; we follow Wait's formulation (Wait, 1996, pp.318-321). The result of this analysis is that the impedance at each layer can be viewed as looking "out" of a non-uniform transmission line. Thus the impedance at each layer is determined by the radius of the layer, the thickness of the layer, the dielectric properties of the layer and the effective impedance above the layer.

In our case we will use layers of uniform thickness ($=h$) and let b_1 be the radius of the lowest layer. So the impedance at each layer can be written as

$$Z_n^{[v]} = \zeta(b_1 + (n-1)h, h, \epsilon_n, Z_{n+1}^{[v]})$$

Where the superscript $[v]$ indicates that this is the impedance for the

v th mode of the conventional solution or the Watson transformed solution.

Clearly one may start at some large value of the radius beyond the ionosphere where $Z_n^{[v]} = Z_0$ and then step inwards layer-by-layer until one is in a region below the ionosphere where the dielectric properties are again those of free space. If the calculation results in a clearly defined impedance layer, then this can be used as a

boundary condition for either the conventional or Watson transformed calculation. The results of one such Watson transformed calculation for a VED at 100 Hz is shown in Figure 7.

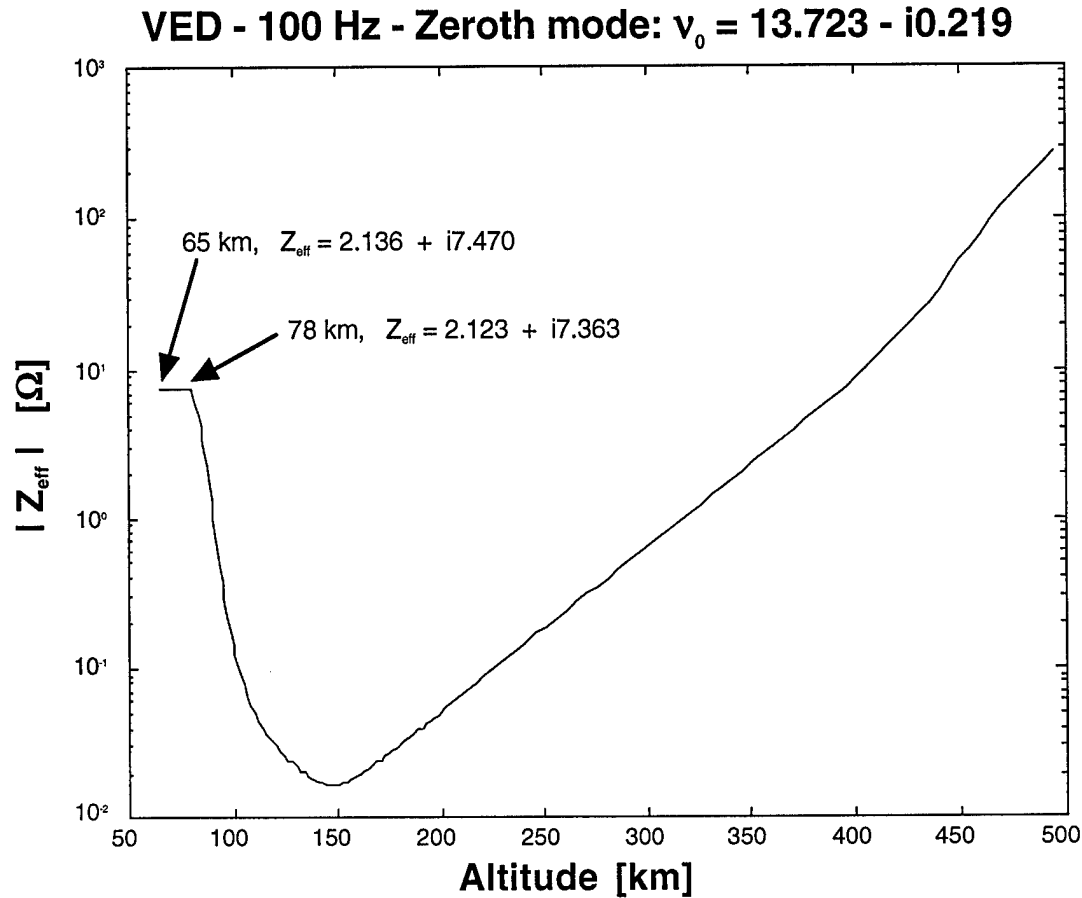
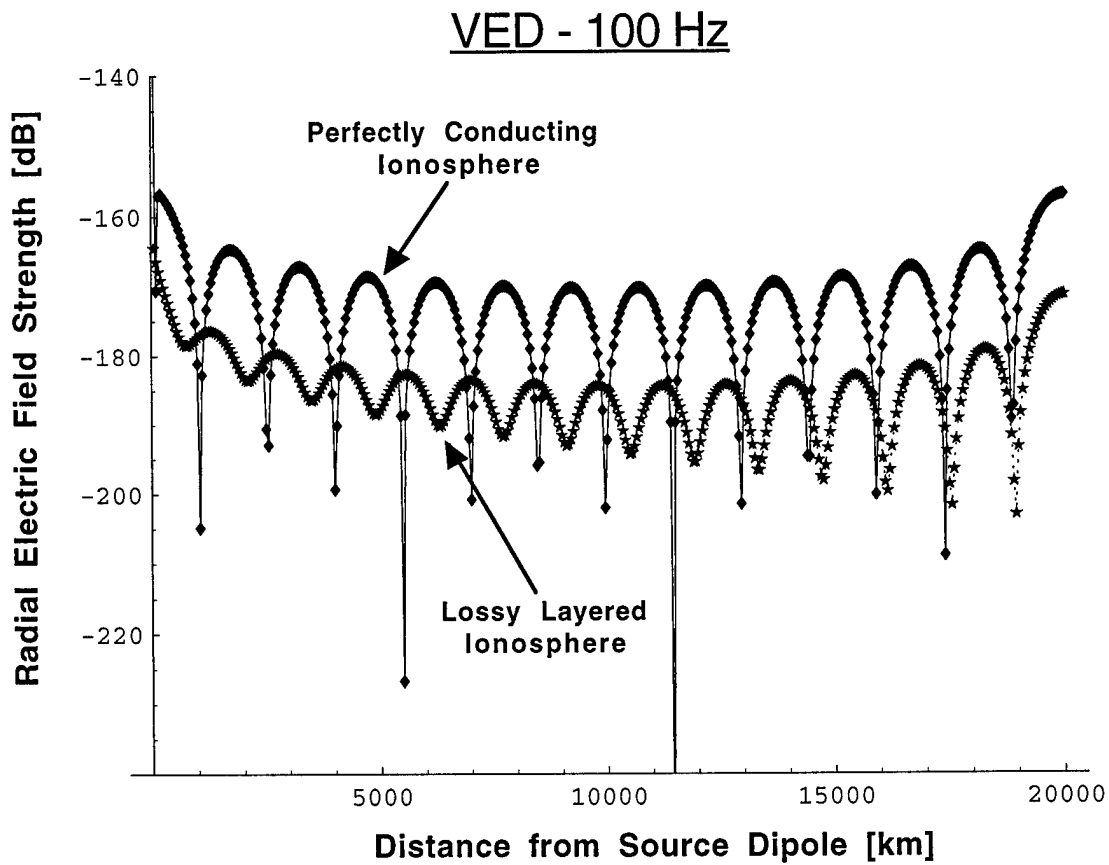


Figure 7: Result of inward iterated layered impedance calculation

The calculation is performed as a sequence of steps

1. Calculate ν_0 (Watson transform complex mode number) for a perfectly conducting ionosphere
2. Use this value of ν_0 ($=12.941$) to calculate the effective impedance using inward iteration to a point well below the ionosphere (in our case 65 km)
3. Use this updated effective impedance and an estimated effective ionosphere height to recalculate ν_0 ($=13.723-i0.219$)
4. Recalculate the the effective impedance using inward iteration to 65 km
5. Estimate the height of the effective impedance layer

This last step is performed by using the equation $Z_2^{[v]} = \zeta(b_2, h_2, \epsilon_2, Z_1^{[v]})$ and assuming a layer whose bottom($= b_2$) is 65 km and whose top($= b_2 + h$) is a test altitude with an effective impedance of $Z_1^{[v]}$. This layer is assumed to have a free space dielectric constant (i.e. $\epsilon_2 = \epsilon_0$). Put in values of heights above 65 km and see where this relation breaks down, i.e. where the value of $Z_2^{[v]}$ is not consistent with the free space dielectric assumption. Just below that point is the estimated effective impedance boundary layer. For our case this effective impedance boundary layer is at 78 km with an effective impedance of $2.123 + i7.363 \Omega$. Using this result we can now calculate the field for this lossy layered ionosphere model and compare with a perfectly conducting ionosphere. This comparison is shown in Figure 8.



**Figure 8: Comparison of the lossy layered ionosphere
with the perfectly conducting ionosphere**

Local Sources

Subsurface structures can be excited by electromagnetic radiation from local, above ground sources such as current loops or electric dipoles. At ELF/VLF these sources can usually be represented by one or more dipole sources: electric dipoles or magnetic dipoles (current loops). This section deals just with the primary fields excited by these local man-made sources above a 2-layer earth as depicted in Figure 9, meaning the fields generated in the absence of an underground structure.

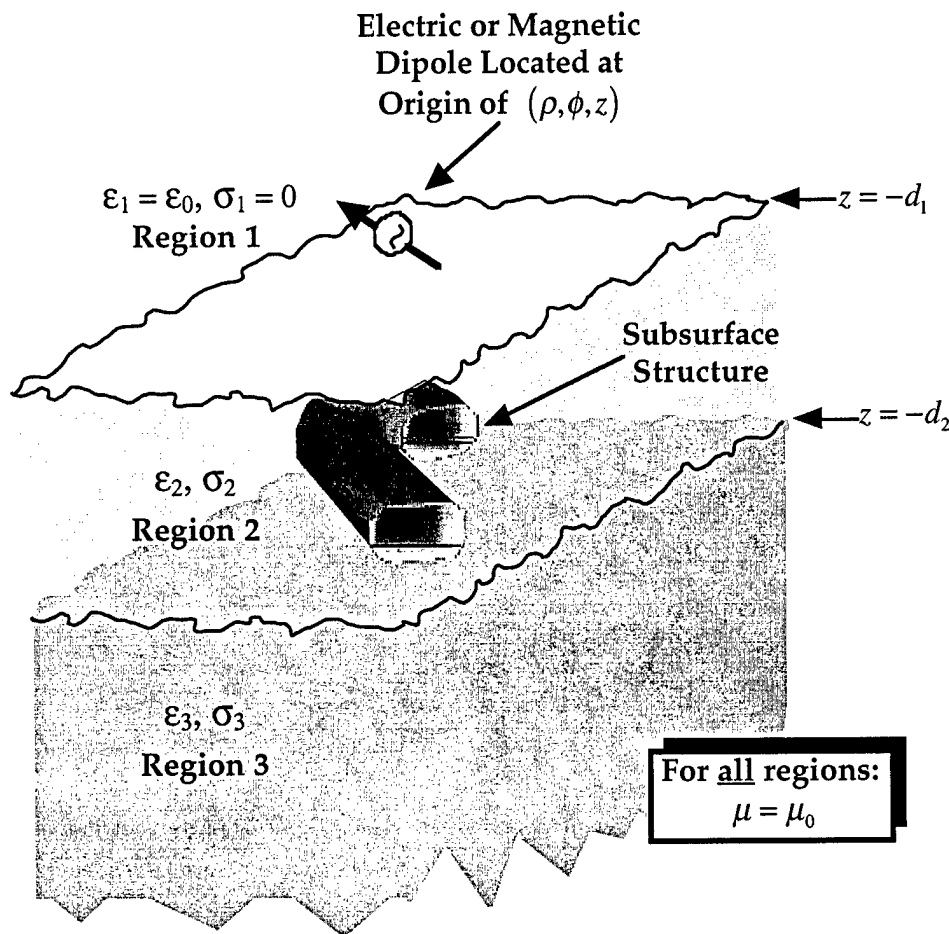


Figure 9: Two layer earth model

The discussion of the perturbed field due to the induced currents on the subsurface structure will be discussed in a later section.

For horizontal or vertical (electric or magnetic) dipoles the vertical components (i.e. along "z-axis") of the fields E_{1z} and H_{1z} above the ground (in region 1) may be

written as (see Chew, 1995, pp.71-79), assuming the source dipole/loop is at the origin of a cylindrical system: (ρ, ϕ, z)

$$F_{1z}^{[1]}(k_1, \rho, \phi, z) = F_{1z}^0(\phi) \int_0^\infty dk_\rho f_F(k_\rho, k_{1z}) J_m(k_\rho \rho) \left[\alpha_F e^{ik_{1z}|z|} + \beta_F \tilde{R}_{12}^F e^{ik_{1z}(z+2d_1)} \right]$$

where

- $F_{1z}^{[1]}$ - Vertical component of the field: E_{1z} or H_{1z} , the [1] superscript indicates that the source is in region 1
- $F_{1z}^0(\phi)$ - Function (may be constant or zero) of the azimuthal angle, ϕ
- k_{1z} - $\sqrt{k_1^2 - k_\rho^2}$, k_1 is the free space (region 1) wave number
- ρ - $\sqrt{x^2 + y^2}$
- $f_F(k_\rho, k_{1z})$ - Function of k_ρ and k_{1z} ($= \sqrt{k_1^2 - k_\rho^2}$)
- m - 0 for VED/VMD and 1 for HED/HMD
- α_F, β_F - Each may be ± 1 depending on dipole orientation/field component
- d_1 - Height of dipole above ground (assumes source at $z = 0$)
- \tilde{R}_{12}^F - Generalized reflection coefficient at 1-2 ground interface

Note: The integrals described in this section and the Perturbed Field Calculations section are all given in detail with needed definitions in Appendix A of this Report.

A similar relation holds for the vertical components of the fields below the ground in region 2 due to the above ground source.

$$F_{2z}^{[1]}(k_1, \rho, \phi, z) = F_{2z}^0(\phi) \int_0^\infty dk_\rho A_2 f_F(k_\rho, k_{1z}) J_m(k_\rho \rho) \left[\alpha_F e^{-ik_{1z}z} + \beta_F \tilde{R}_{23}^F e^{ik_{1z}(z+2d_2)} \right]$$

The definitions are similar to above except that d_2 is the height of the dipole above the 2-3 interface and the introduction of the coefficient A_2 related to the generalized transmission coefficient through the 1-2 interface.

The transverse field can be obtained from the vertical fields via the following ansatz (Chew, 1995, pp. 75-76). Observe that we can write the electric and magnetic fields within a given layer as integral transforms:

$$\mathbf{E}(\mathbf{r}) = \int_0^\infty dk_\rho \tilde{\mathbf{E}}(\mathbf{r}, k_\rho) \quad \text{and} \quad \mathbf{H}(\mathbf{r}) = \int_0^\infty dk_\rho \tilde{\mathbf{H}}(\mathbf{r}, k_\rho)$$

where

$$\tilde{\mathbf{E}}(\mathbf{r}, k_\rho) = \tilde{\mathbf{E}}_t(\mathbf{r}, k_\rho) + \hat{\mathbf{z}} \tilde{E}_z(\mathbf{r}, k_\rho) \quad \text{and} \quad \tilde{\mathbf{H}}(\mathbf{r}, k_\rho) = \tilde{\mathbf{H}}_t(\mathbf{r}, k_\rho) + \hat{\mathbf{z}} \tilde{H}_z(\mathbf{r}, k_\rho)$$

Chew shows that

$$\begin{bmatrix} \tilde{\mathbf{E}}_t \\ \tilde{\mathbf{H}}_t \end{bmatrix} = \frac{1}{\omega^2 \mu \epsilon - k_z^2} \begin{bmatrix} \nabla_t \frac{\partial}{\partial z} & -i\omega \mu \hat{\mathbf{z}} \times \nabla_t \\ i\omega \epsilon \hat{\mathbf{z}} \times \nabla_t & \nabla_t \frac{\partial}{\partial z} \end{bmatrix} \begin{bmatrix} \tilde{E}_z \\ \tilde{H}_z \end{bmatrix}, \quad \text{where } \nabla_t \equiv \nabla - \hat{\mathbf{z}} \frac{\partial}{\partial z}$$

The expressions for $\tilde{\mathbf{E}}_t$ and $\tilde{\mathbf{H}}_t$ may then be integrated to obtain the transverse components of the fields.

As an example of this type of calculation consider a 1 meter radius current loop

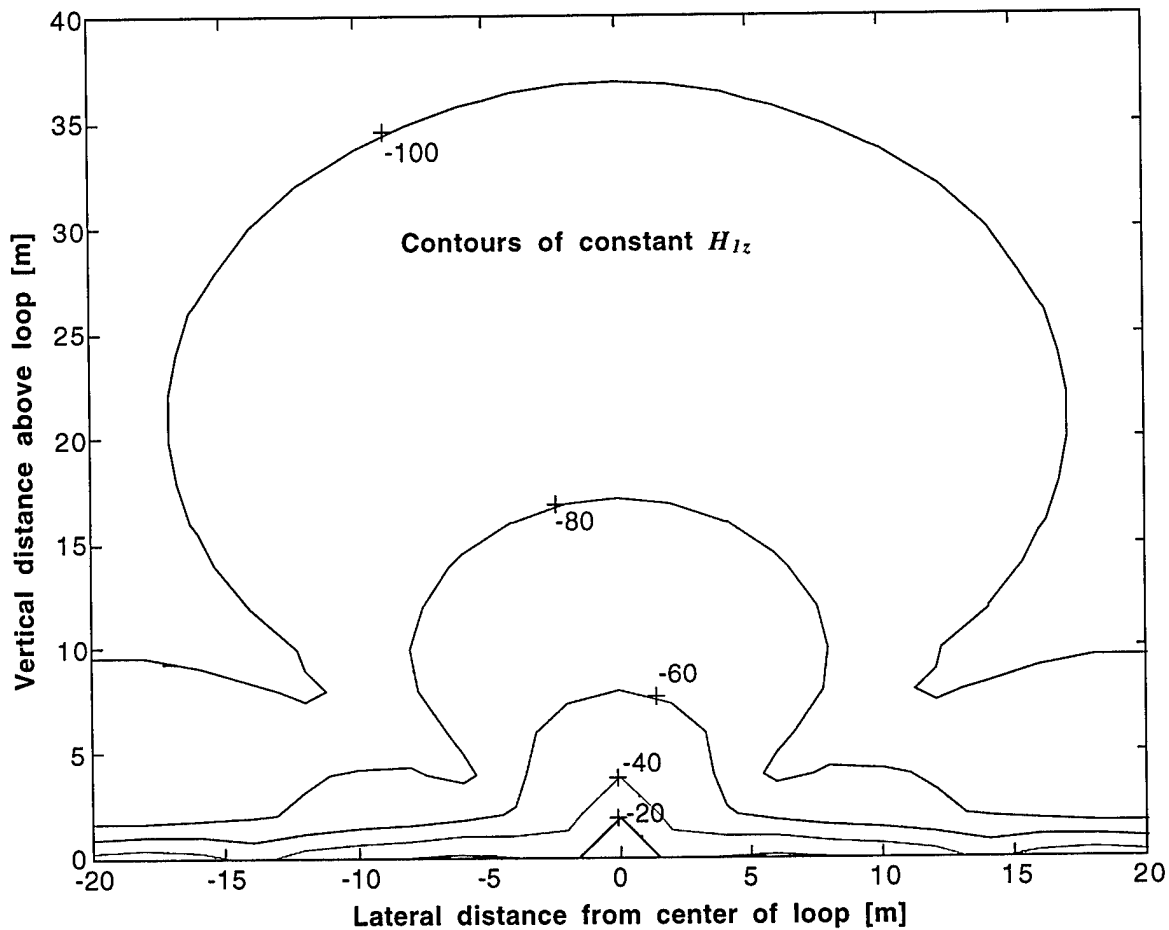


Figure 10: Contour plot for constant values of H_{1z} in dB-amp/m. The source frequency is 3 kHz; the source is a 1 meter radius current loop (1 amp). The loop is 1 meter above a two layer earth with properties given in the text.

(VMD) above the ground at a height of 1 meter($\Rightarrow d_1 = 1$ meter); assume a frequency of 3 kHz with ground properties of:

$$\frac{\epsilon_1}{\epsilon_0} = 10, \sigma_1 = 0.01 \text{ mhos/m} \text{ and } \frac{\epsilon_2}{\epsilon_0} = 20, \sigma_2 = 0.02 \text{ mhos/m}$$

and the thickness of the layer is 100 meters ($\Rightarrow d_2 = 101 \text{ meters}$). The magnetic field above ground can be written as

$$H_{1z} = \frac{-iIa^2}{4} \int_0^\infty dk_\rho \frac{k_\rho^3}{k_{1z}} J_0(k_\rho \rho) \left[e^{ik_{1z}|z|} + \tilde{R}_{12}^{TE} e^{ik_{1z}(z+2d_1)} \right]$$

where $a (=1 \text{ meter})$ is the radius of the loop, I is the current in the loop (for simplicity we will assume 1 amp), and

$$\tilde{R}_{12}^{TE} = \frac{(k_{1z} - k_{2z})(k_{2z} + k_{3z}) + (k_{1z} + k_{2z})(k_{2z} - k_{3z})e^{2ik_{2z}(d_2 - d_1)}}{(k_{1z} + k_{2z})(k_{2z} + k_{3z}) + (k_{1z} - k_{2z})(k_{2z} - k_{3z})e^{2ik_{2z}(d_2 - d_1)}}$$

with

$$k_{mz} = \sqrt{k_m^2 - k_\rho^2} = \sqrt{\left(\frac{\epsilon_m}{\epsilon_0} + i \frac{\sigma_m}{\omega \epsilon_0} \right) k_1^2 - k_\rho^2}$$

Carrying out the integration, we obtain the contour plot shown in Figure 10 for the H_{1z} primary field above ground.

Frequency Dependence

Optimizing any sensor system requires a knowledge of the frequency dependence of the system and hence the various components of that system. Below we plot the frequency dependence of the source field only; in subsequent sections appropriate plots of frequency dependence of the other components will be presented.

The plot below depicts the frequency dependence of fields from a VMD source (i.e., a small loop) 1 meter above a specified two-layer earth as observed at two points: 1) a point 1.66 meters displaced horizontally from the source above the earth-air interface and 2) a point 3 meters below the earth-air interface at a horizontal distance of 2 meters. The 1.66 meters is chosen to reflect the distance from the source to receiver distance of the sensor system selected for analysis (GEM-2 from Geophex, see below). The quantities plotted are the in-phase (real) and quadrature (imaginary) values of the z-axis component of the B-field in picoTesla. The VMD source is a 3 amp-m² magnetic dipole (consistent with the GEM-2). Again we use a two-layer earth with ground properties of:

$$\frac{\epsilon_1}{\epsilon_0} = 10, \sigma_1 = 0.01 \text{ mhos/m} \text{ and } \frac{\epsilon_2}{\epsilon_0} = 20, \sigma_2 = 0.02 \text{ mhos/m}$$

and the thickness of the layer is 100 meters.

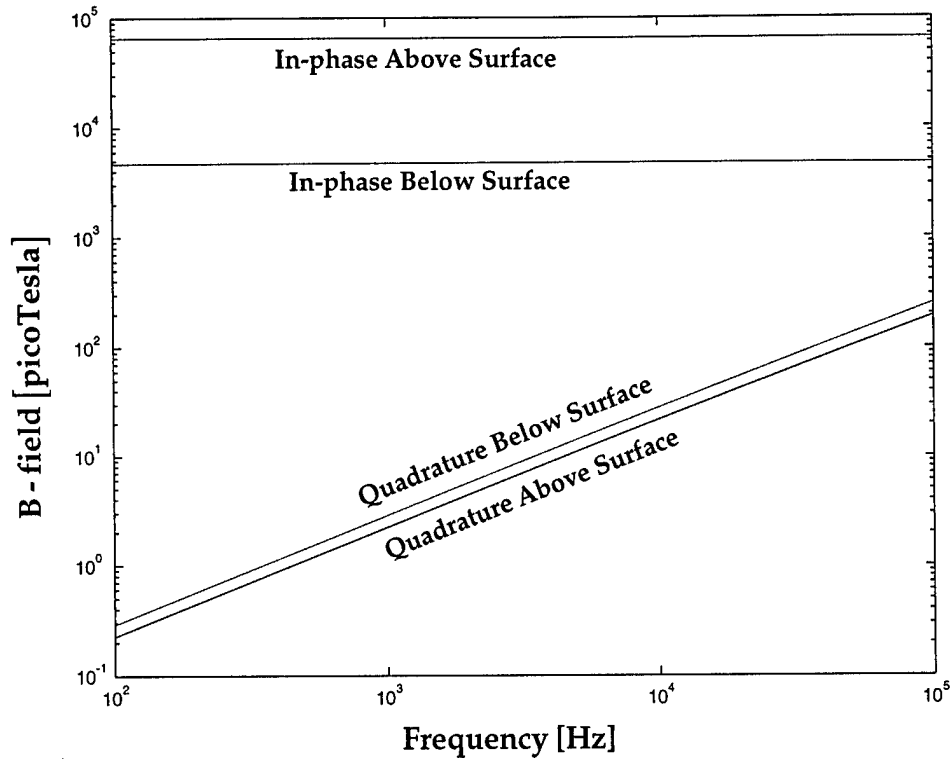


Figure 11: Frequency dependence of the in-phase (real) and quadrature (imaginary) values of the z-axis component of the B-field for two points relative to a magnetic moment source of 3 amp-m². 1) A point 1.66 meters from the source above the earth-air interface and 2) A point 3 meters below the earth-air interface at a horizontal distance of 2 meters from the source

One surprising result of these calculations is that the below ground quadrature field is slightly larger than the the above ground quadrature field, even though the distance to the source is larger for the below ground point than the above ground point - 4.47 meters vs. 1.66 meters. We do not have an explanation for this at this point, although it might help in sensor design/optimization.

Natural Sources - External Noise

A crucial component in establishing the feasibility of a sensor system are the signals always present in the natural environment. Lightning strokes around the earth (100 per second, on average) fill the earth-ionosphere cavity with "noise" that has approximately a $1/f$ field-strength dependence on frequency, down to ~ 0.1 Hz (Fraser-Smith et al., 1991; Lanzerotti et al., 1990). The precise relationship based on a fit to the experimental data and referenced to 10 Hz is:

$$\langle B_{Noise} \rangle = 0.5 \left(\frac{f}{10} \right)^{-1.2}$$

where $\langle B_{Noise} \rangle$ is the rms magnetic field average external noise for a 1 Hz bandwidth in the atmosphere in picoTesla / $\sqrt{\text{Hz}}$ and f is the frequency in Hz. This relationship between the rms magnetic field average and frequency is plotted in Figure 12, below.

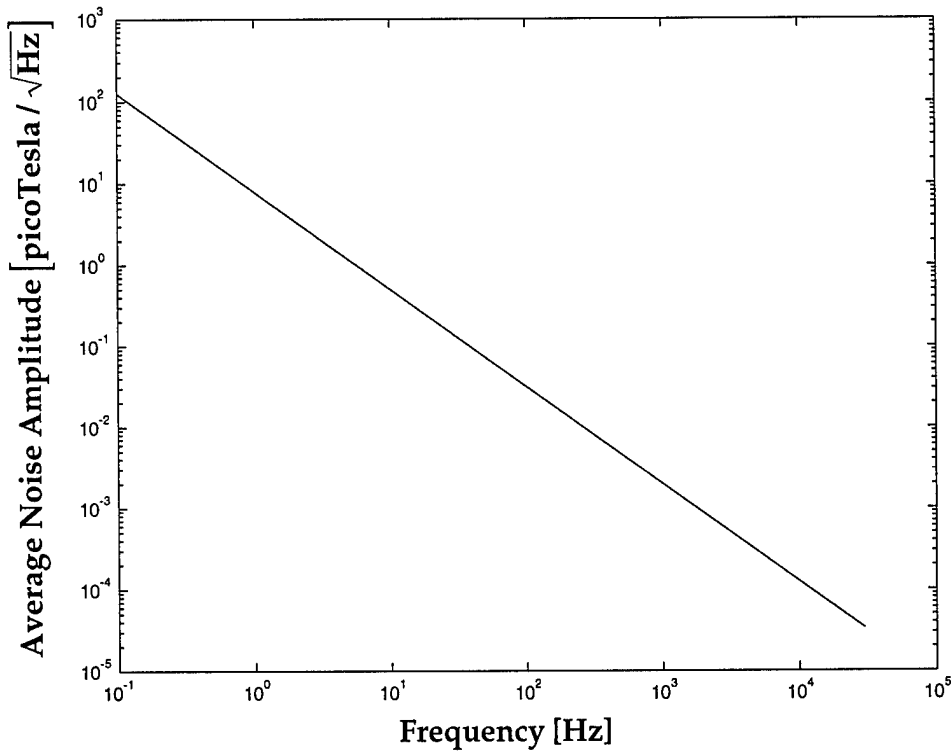


Figure 12: Plot of the amplitude of the rms B-field average external noise in picoTesla / $\sqrt{\text{Hz}}$

Underground Structure Modeling

The underground structures will in most cases be much smaller than the wavelength (even the shortened effective wavelength due to the ground dielectric properties). This fact allows us to model the underground structures as magnetic and electric dipoles. In this section we will define and discuss these dipoles and two approaches to calculating these dipoles: NEC-3 and an ellipsoid dipole model. For the ellipsoid dipole model we give the values of the dipole moments when excited by an external field (electric or magnetic).

Dipole Definitions and the Long Wavelength Approximation

Electric Dipole Moment

The electric dipole moment, \mathbf{p} , of a localized charge distribution, $\rho(\mathbf{r})$, is defined as

$$\mathbf{p} = \int_V (\mathbf{R}_0 + \mathbf{r}) \rho(\mathbf{r}) d^3r$$

where \mathbf{R}_0 is the radius vector from the coordinate system origin to the center of the charge distribution and V is the region containing the charge distribution. This definition holds for any frequency.

Assume: 1) the structure scale is much shorter than the wavelength of the exciting radiation (Long Wavelength Approximation), 2) all dimensions stay comparable, 3) material properties stay finite, and 4) the structure does not have its own sources, then we can write

$$\mathbf{p} \cong \beta_0 V$$

So the dipole moment will linearly proportional to the volume of the subsurface structure; this will be seen in more detail below.

If the field is not static, then we can write (using current conservation and some vector calculus) with \mathbf{J} being the current density and ω the radian frequency.

$$\mathbf{p} = \frac{i}{\omega} \int_V \mathbf{J}(\mathbf{r}) d^3r$$

As a check we consider a localized current source along the z-axis from $-L/2$ to $L/2$

$$\begin{aligned} \mathbf{p} &= \frac{i}{\omega} \int_V \mathbf{J}(\mathbf{r}) d^3r = \hat{\mathbf{z}} \frac{i}{\omega} \int_V I_0 \delta(x) \delta(y) \theta\left(\frac{L}{2} - |z|\right) dx dy dz \\ &= \hat{\mathbf{z}} I_0 L \frac{i}{\omega} \end{aligned} \quad \left\{ \begin{array}{l} \theta(u) = \text{Unit pulse function} = \begin{cases} 1 & u \leq 1 \\ 0 & u > 1 \end{cases} \\ \delta(u) = \text{Dirac-delta function} \end{array} \right.$$

This is consistent with the usual notions of an electric dipole moment.

Magnetic Dipole Moment

The magnetic dipole moment is defined as

$$\mathbf{m} = \frac{1}{2} \int_V (\mathbf{R}_0 + \mathbf{r}) \times \mathbf{J}(\mathbf{r}) d^3r$$

and, again, using the Long Wavelength Approximation and assuming no underground sources we have the approximate relation

$$\mathbf{m} \equiv \xi_0 V$$

Again the magnetic dipole moment is linearly proportional to the volume of the subsurface structure.

As a check we consider a current loop in the x-y plane at the origin or

$$\mathbf{J}(\mathbf{r}) = \hat{\phi} I \delta(r - a) \delta(\cos \theta)$$

so

$$\begin{aligned} \mathbf{m} &= \frac{1}{2} \int_V \mathbf{r} \times \hat{\phi} I \delta(r - a) \delta(\cos \theta) d^3r = \frac{I}{2} \int_V \hat{\mathbf{z}} r \delta(r - a) r^2 dr \delta(\cos \theta) \sin \theta d\theta d\phi \\ &= I \pi a^3 \hat{\mathbf{z}} \end{aligned}$$

Which is consistent with the usual notions for the magnetic dipole moment of a current loop.

NEC-3 Models

The most general approach to modeling a conducting underground structure is to use a method-of-moments wire grid model. This approach although powerful does require some care at low frequencies (NEC was developed with the resonance region in mind). There are some technical difficulties for structures whose feature size is $< 10^{-3} \lambda$. Use of NEC will be restricted to structures that are not too small, and where its capabilities are required to adequately describe its electromagnetic response; in other cases we will use dipole ellipsoid models (see following section).

Ellipsoid Dipole Models

Ellipsoid Geometry

In this effort we wish to model a variety of underground structures: rectangular boxes, cylinders, spheres. If the structure does not exceed the Long Wavelength Approximation, it may be adequately represented as an oriented ellipsoid. An ellipsoid is defined by the values of its three semiprincipal axes: a_1, a_2, a_3 . Below in Figure 13 is a sketch of this solid.

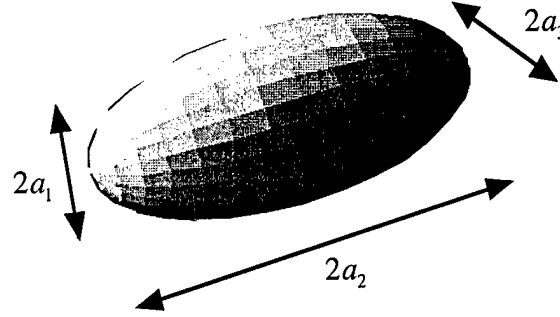


Figure 13: Ellipsoid Dipole model

The volume of this solid is $V = \frac{4\pi}{3} a_1 a_2 a_3$. This model will be used for both the electric and magnetic dipole structures.

Induced Dipole Moment Values in the Static Limit

In the static limit, the induced electric dipole moment on an ellipsoid due to an external electric field $\mathbf{E}_0 = \hat{\mathbf{x}}E_{0x} + \hat{\mathbf{y}}E_{0y} + \hat{\mathbf{z}}E_{0z}$ can be written as (Stratton, pp207-213)

$$\mathbf{p} = \frac{4\pi a_1 a_2 a_3}{3} \left(\hat{\mathbf{x}} \frac{(\epsilon_{struct} - \epsilon_0)E_{0x}}{1 + \frac{a_1 a_2 a_3}{2\epsilon_2}(\epsilon_{struct} - \epsilon_2)A_x} + \hat{\mathbf{y}} \frac{(\epsilon_{struct} - \epsilon_0)E_{0y}}{1 + \frac{a_1 a_2 a_3}{2\epsilon_2}(\epsilon_{struct} - \epsilon_2)A_y} + \hat{\mathbf{z}} \frac{(\epsilon_{struct} - \epsilon_0)E_{0z}}{1 + \frac{a_1 a_2 a_3}{2\epsilon_2}(\epsilon_{struct} - \epsilon_2)A_z} \right)$$

where

- ϵ_{struct} - Effective dielectric constant of the structure
- ϵ_2 - Dielectric constant of medium surrounding the structure (see Fig. 9)
- A_x, A_y, A_z - Functions that depend on all three semiprincipal axes - are , in general, elliptic integrals; for a sphere $A_x = A_y = A_z = \frac{4}{3}a^3$

Clearly $\mathbf{p} \propto \frac{4\pi a_1 a_2 a_3}{3}$ as expected from our Long Wavelength Approximation analysis above.

For a sphere this reduces to

$$\mathbf{p} = 4\pi a_0^3 \frac{\epsilon_2(\epsilon_{struct} - \epsilon_0)}{2\epsilon_2 + \epsilon_{struct}} \mathbf{E}_0$$

We can write for an external magnetic field $\mathbf{H}_0 = \hat{\mathbf{x}}H_{0x} + \hat{\mathbf{y}}H_{0y} + \hat{\mathbf{z}}H_{0z}$ (see Stratton, p258)

$$\mathbf{m} = \frac{4\pi a_1 a_2 a_3}{3\mu_0} \left(\hat{\mathbf{x}} \frac{(\mu_{struct} - \mu_0)H_{0x}}{1 + \frac{a_1 a_2 a_3}{2\mu_2}(\mu_{struct} - \mu_2)A_x} + \hat{\mathbf{y}} \frac{(\mu_{struct} - \mu_0)H_{0y}}{1 + \frac{a_1 a_2 a_3}{2\mu_2}(\mu_{struct} - \mu_2)A_y} + \hat{\mathbf{z}} \frac{(\mu_{struct} - \mu_0)H_{0z}}{1 + \frac{a_1 a_2 a_3}{2\mu_2}(\mu_{struct} - \mu_2)A_z} \right)$$

where

- μ_{struct} - Effective permeability of the structure
 μ_2 - Permeability of medium surrounding the structure (for our study this is μ_0)

For a sphere

$$\mathbf{m} = 4\pi a_0^3 \frac{\mu_2}{\mu_0} \left[\frac{\mu_{struct} - \mu_0}{2\mu_2 + \mu_{struct}} \right] \mathbf{H}_0$$

The above relations for magnetic dipole moments are only important when the structure has a permeability different from μ_0 ; this is not true in many cases. But this result is useful in checking the static limit (see below) of the very important result concerning the induced magnetic dipole moment on a conducting ellipsoid.

Induced Magnetic Dipole Moment Values of a Conducting Sphere

Wait (1951, 1968) has examined the frequency dependence of the induced magnetic

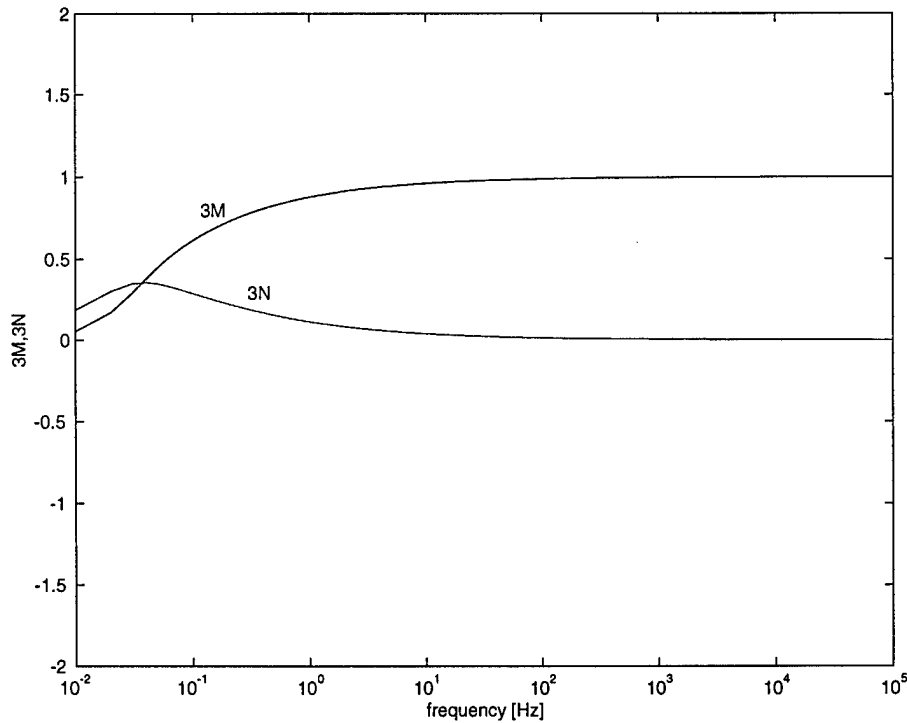


Figure 14: Frequency dependence of the functions used in calculating the induced magnetic dipole for a 1 meter radius aluminum sphere

dipole moment of a conducting sphere in a medium. He obtains the following result

$$\mathbf{m} = -2\pi a_0^3 (3M + iN) \mathbf{H}_0$$

where

$$3M + i3N = -\frac{2\mu_{struct}(\sinh\gamma - \gamma \cosh\gamma) + \mu_0(\sinh\gamma - \gamma \cosh\gamma + \gamma^2 \sinh\gamma)}{\mu_{struct}(\sinh\gamma - \gamma \cosh\gamma) - \mu_0(\sinh\gamma - \gamma \cosh\gamma + \gamma^2 \sinh\gamma)} \mathbf{H}_0$$

with $\gamma = a_0 \sqrt{-i\omega\sigma\mu_{struct}}$. In Figure 14 $3M$ and $3N$ are plotted as a function of frequency for a 1 meter radius aluminum sphere ($\sigma_{Al} = 3.82 \times 10^7$ mhos/m and $\mu_{Al} = 1.00000065\mu_0$). In Figure 15 $3M$ and $3N$ are plotted as a function of frequency for a 1 meter radius iron sphere ($\sigma_{Al} = 1.03 \times 10^7$ mhos/m and $\mu_{Al} = 90\mu_0$).

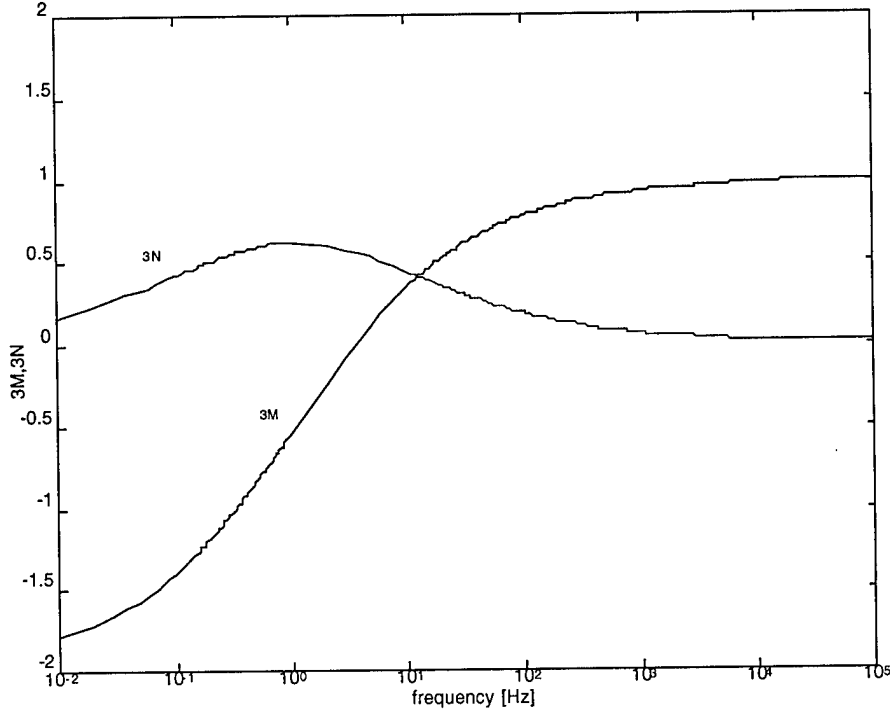


Figure 15: Frequency dependence of the functions used in calculating the induced magnetic dipole for a 1 meter radius iron sphere

If we examine the static limit (i.e. let $\gamma \rightarrow 0$) and the permeability of the surrounding medium is μ_0 we recover the value obtained previously:

$$\mathbf{m} = 4\pi a_0^3 \left[\frac{\mu_{struct} - \mu_0}{2\mu_0 + \mu_{struct}} \right] \mathbf{H}_0.$$

For iron ($\mu_{Al} = 90\mu_0$) this static limit evaluates to

$$\mathbf{m} = 4\pi a_0^3 \left[\frac{89\mu_0}{92\mu_0} \right] \mathbf{H}_0 = 2\pi a_0^3 [1.935] \mathbf{H}_0$$

$$\Rightarrow 3M + i3N = -1.935$$

consistent with Figure 15.

Finally it is useful to look at the frequency dependence of the scale variation, i.e.

what happens for various size spheres as a function of frequency. Figure 16 shows $3M$ and $3N$ for various radii iron spheres.

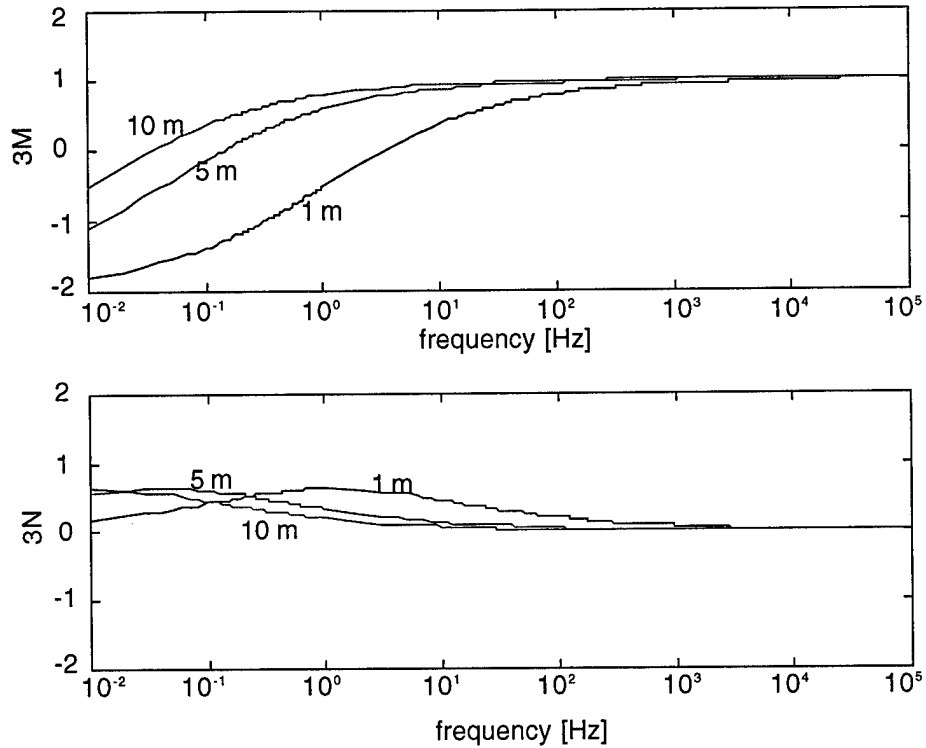


Figure 16: Frequency dependence of the functions used in calculating the induced magnetic dipole for various radii iron spheres

It is clear from this plot that for frequencies > 100 Hz the magnetic dipole moment of an iron sphere of radius > 1 meter approaches the asymptotic limits of $3M \rightarrow 1$ and $3N \rightarrow 0$, i.e. $\mathbf{m} \equiv -2\pi a_0^3 \mathbf{H}_0$.

Perturbed Field Calculations

When the subsurface structure has been excited by electromagnetic radiation from the above ground sources (local or remote) we can approximate the excited structure as a magnetic and/or electric dipole moment. The value of this dipole moment was discussed in the previous section. In this section we outline the form of the calculations required to obtain the above ground field due to this dipole. The field due to this dipole is called the perturbed field. Figure 17 shows a sketch of the situation.

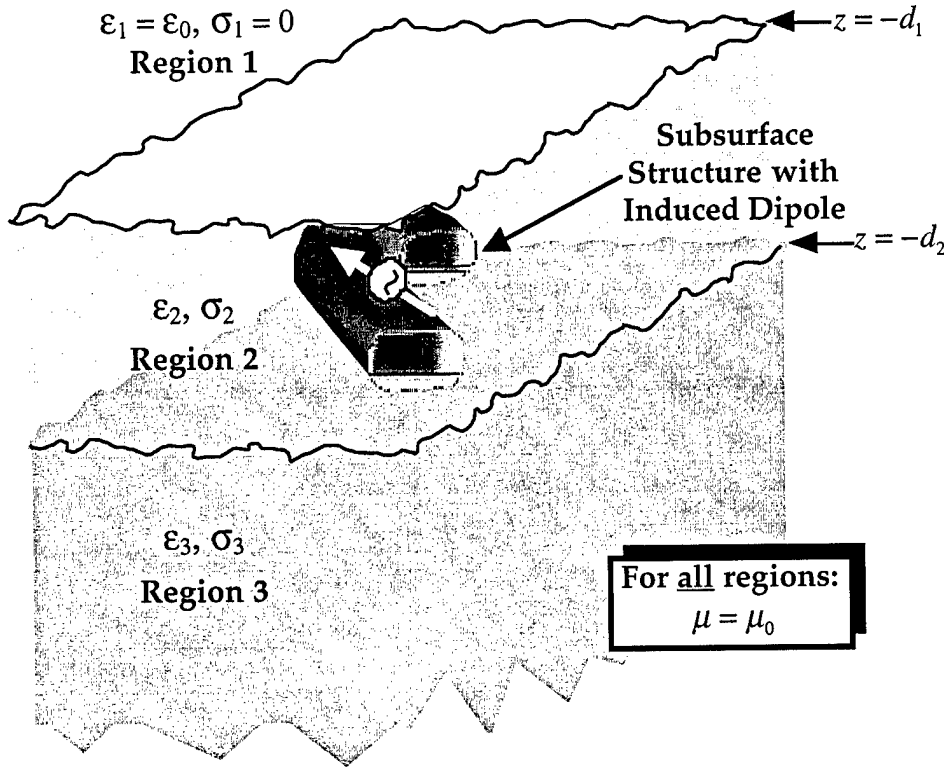


Figure 17: Induced dipole due below ground structure and external field

The above ground (Region 1) E and H fields due to an arbitrarily oriented dipole in the first layer (Region 2 of the sketch) of a 2-layer earth problem can be written as Sommerfeld integrals. As before one need only formulate the integrals for E_{2z} and H_{2z} and then obtain the transverse components via differentiation. These integrals may be written as (see Chew, pp71-79)

$$F_{2z}^{[2]}(k_1, k_2, \rho, \phi, z) = G_{2z}^0(\phi) \int_0^\infty dk_\rho g_F(k_\rho, k_{1z}, k_{2z}) J_m(k_\rho \rho) \left[e^{-ik_{2z}z'} + \tilde{R}_{23}^F e^{ik_{2z}(z'+2d_2)} \right]$$

where

- $F_{2z}^{[2]}$ - Vertical component of the field: E_{2z} or H_{2z} , the [2] superscript indicates that the source is in region 2
- $G_{2z}^0(\phi)$ - Function (may be constant or zero) of the azimuthal angle, ϕ
- k_{2z} - $\sqrt{k_2^2 - k_\rho^2}$, $k_2 = \sqrt{\frac{\epsilon_2}{\epsilon_0}} k_1$ is the region 2 wave number
- ρ - $\sqrt{x^2 + y^2}$
- $g_F(k_\rho, k_{1z}, k_{2z})$ - Function of k_ρ , k_{1z} , and k_{2z} includes the generalized transmission coefficient through the 1-2 interface
- m - 0 for VED/VMD and 1 for HED/HMD
- d_2 - Negative z value of the bottom of Region 2 layer (see Figure 13)
- z' - Location of dipole below ground
- \tilde{R}_{23}^F - Generalized reflection coefficient at 2-3 ground interface

Again the dipole/loop is situated along the z -axis of a (ρ, ϕ, z) system.

Figure 18 gives results for the above ground field due to a typical below ground source (1 Amp-m²) - two-layer earth with ground properties of:

$$\epsilon_1 = 10\epsilon_0, \sigma_1 = 0.01 \text{ mhos/m and } \epsilon_2 = 20\epsilon_0, \sigma_2 = 0.02 \text{ mhos/m}$$

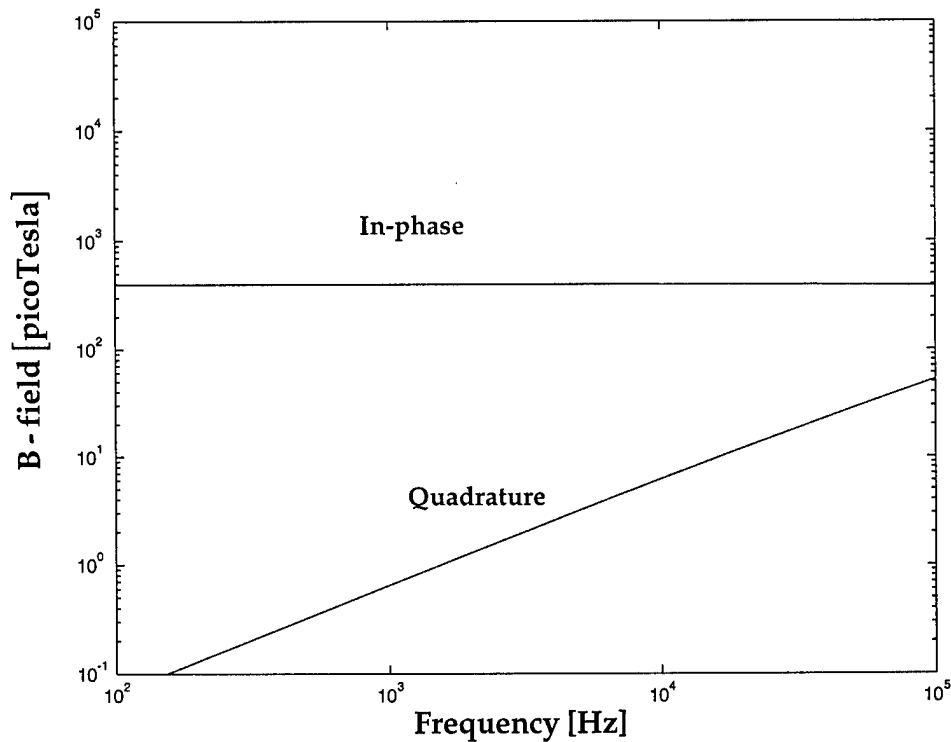
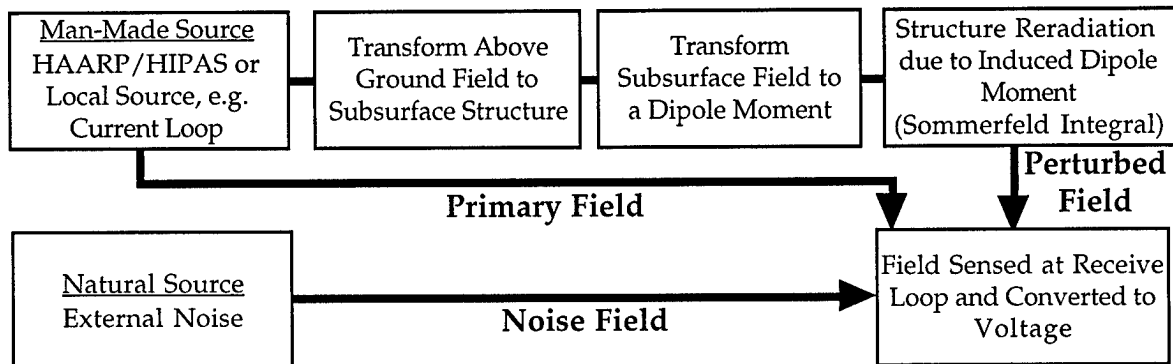


Figure 18: Plot of the z -axis B-field for a below ground VMD source (1 amp-m²) at an above ground point. The below ground VMD is 3 meters below the surface. The point above ground is 1 meter above the surface and at a horizontal distance of 3.66 meters from the below ground source.

Total Field Calculation

This section will review the relation between the source excitation and the received signal (open circuit voltage) at an ideal N-turn loop sensor. The sources considered will be those given above: remote man-made, local man-made, and natural sources. The description will be in terms of a flow of signal from source to receiver analogous to the "Radar Range Equation".

The flow of signal from source to receiver is as shown below:



The first point to note is that the signal at the receiver is the result of a coherent sum of three fields: the primary field directly from the source, the perturbed field due to the underground structure, and the external noise due to various natural sources. These have all been described earlier; below we will review each of these in a summary of the calculations described in previous sections.

- **Man-Made Source**

The source is expressed in terms of an electric or magnetic dipole moment, whose location and orientation over the earth is specified by the user. This source may be local or remote. Previous sections describe the calculation of these primary fields.

- **External Noise**

The fields due to external noise will be coded into a look-up table.

- **Transform Above Ground Fields to Subsurface Structure**

Remote Sources: The above ground fields in the vicinity of the source are used along with the ground properties to obtain the below ground fields. This is quite simple since the wavelengths are long and hence the field variation from above ground to below ground is dependent mostly on the ground

properties.

Local Sources: The below ground fields are calculated in a straightforward way using the Sommerfeld integrals described earlier.

- **Transform Incident Field to a Dipole Moment**

Model the underground structure as an electric and/or magnetic dipole. This can be done simply by approximating its shape as an ellipsoid or by using a method-of-moments code such as NEC.

- **Structure Reradiation due to Induced Dipole Moment**

Once the structure is represented as effective electric or magnetic dipoles, then that result along with the dipole's location and the properties of the two-layer earth are used with the usual Sommerfeld integrals to obtain the above ground field due to the induced dipole moments of the subsurface structure. This is the perturbed field.

- **Field Sensed at Receive Loop and Converted to Voltage**

At the receive sensor (assumed to be an N-turn loop, but not restricted to this) the total field (a coherent sum of the primary field, the noise field, and the perturbed field) excites a voltage across the loop that is then measured.

As an example of these calculations we examine the following situation (Figure 19)

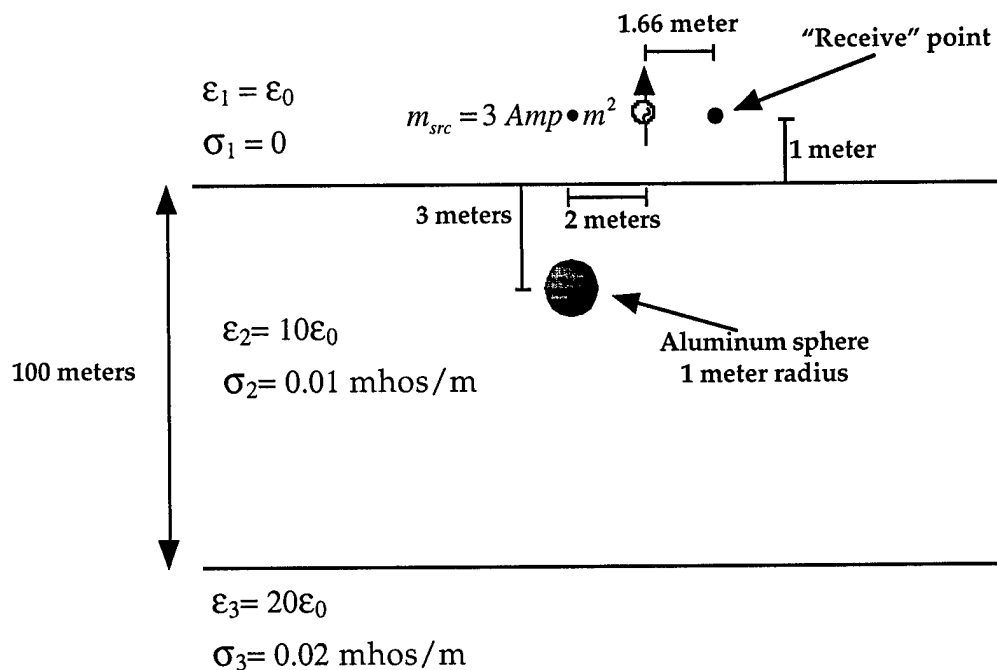


Figure 19

As in previous calculations we use a two-layer earth with ground properties of:

$$\epsilon_1 = 10\epsilon_0, \sigma_1 = 0.01 \text{ mhos/m and } \epsilon_2 = 20\epsilon_0, \sigma_2 = 0.02 \text{ mhos/m}$$

For all regions $\mu = \mu_0 = 4\pi \times 10^{-7}$. The first layer of the earth is 100 meters thick.

One meter above the earth is a 3 amp-m² VMD source. In the first layer of the earth is an aluminum sphere at a depth of 3 meters and with a radius of 1 meter. The horizontal separation between the source and the sphere is 2 meters. We will examine the H-field at a point 1.66 meters in horizontal separation from the source and at the same height as the source; the horizontal distance from this "receive" point to the sphere is 3.66 meters (2 m + 1.66 m). The values in this example are motivated by the specific system we will be analyzing (see below).

For illustrative purposes, we will now use the results as represented in Figures 11, 14, and 18 to calculate the primary field (due to only the source) and the secondary field (due to the induced dipole on the sphere) at the "receive" point. We will only consider the z-axis component of the H-field for this example². We will use a frequency of 1 kHz. All of these calculations are done with the MATLAB code that is to be available to the community in the course of this SBIR program.

Primary Field

The primary magnetic field at the "receive" point due to the source is (at 1 kHz, Figure 11)

$$B_{\text{primary}} = (-65584 + i2.2400) \times 10^{-12} \text{ Tesla} \Rightarrow H_{\text{primary}} = (-52.19 + i0.001783) \times 10^{-3} \frac{\text{Amp}}{\text{m}}$$

$$\text{Recall } H_{\text{primary}} = \frac{B_{\text{primary}}}{\mu_0}$$

Induced Dipole Moment

The magnetic field at the below ground sphere due to the source is (at 1 kHz, Figure 11)

$$B_{\text{ind}} = (4696 + i2.874) \times 10^{-12} \text{ Tesla} \Rightarrow H_{\text{ind}} = (3.737 + i0.002287) \times 10^{-3} \frac{\text{Amp}}{\text{m}}$$

The value of $3M + i3N$ for a 1 meter aluminum sphere at 1 kHz is (Figure 16)

$$3M + i3N = 0.9961 + i0.003853$$

² The offset source does induce horizontal dipole moments in this case - these will be included in the evaluation of the candidate Geophex sensor (below), but for simplicity will not be discussed in this calculation.

So the induced magnetic moment is (with $a_{sphere}=1$ meter)

$$m_{ind} = -2\pi a_{sphere}^3 (3M + i3N) H_{ind} = -(0.02339 + i0.0001048) \text{Amp} \cdot m^2$$

Secondary Field

The magnetic field at the above ground "receive" point due to a 1 Amp-m² below ground (induced) source is (at 1 kHz, Figure 18)

$$B_1 = (397.1 + i0.6484) \times 10^{-12} \text{ Tesla} \quad \Rightarrow \quad H_1 = (0.3160 + i0.00005159) \times 10^{-3} \frac{\text{Amp}}{m}$$

so for a $m_{ind} = -(0.02339 + i0.0001048) \text{Amp} \cdot m^2$ source, the secondary field is

$$B_{2ndry} = -(9.287 + i0.05677) \times 10^{-12} \text{ Tesla} \quad \Rightarrow \quad H_{2ndry} = -(7.390 + i0.04517) \times 10^{-6} \frac{\text{Amp}}{m}$$

Primary to Secondary Field Ratio

The ratio of the secondary to primary magnetic field at the above ground "receive" point for the previously described situation at 1 kHz is

$$\frac{H_{2ndry}}{H_{primary}} = -(141.6 + i0.8704) \times 10^{-6}$$

If this calculation is carried out for a number of frequencies we obtain the results plotted in Figure 20

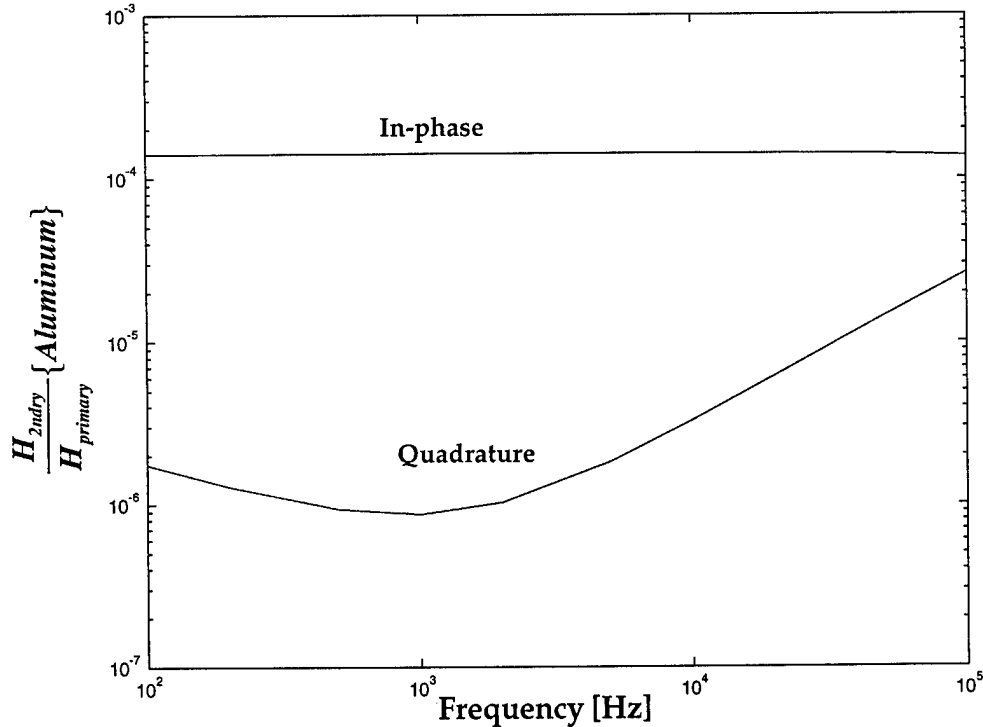


Figure 20: Plot of the secondary to primary z-axis H-field ratio at the "receive" point due to the induced z-axis VMD for the configuration given in Figure 19 with an aluminum sphere (high conductivity).

A similar plot can be made for an iron sphere, this is shown in Figure 21.

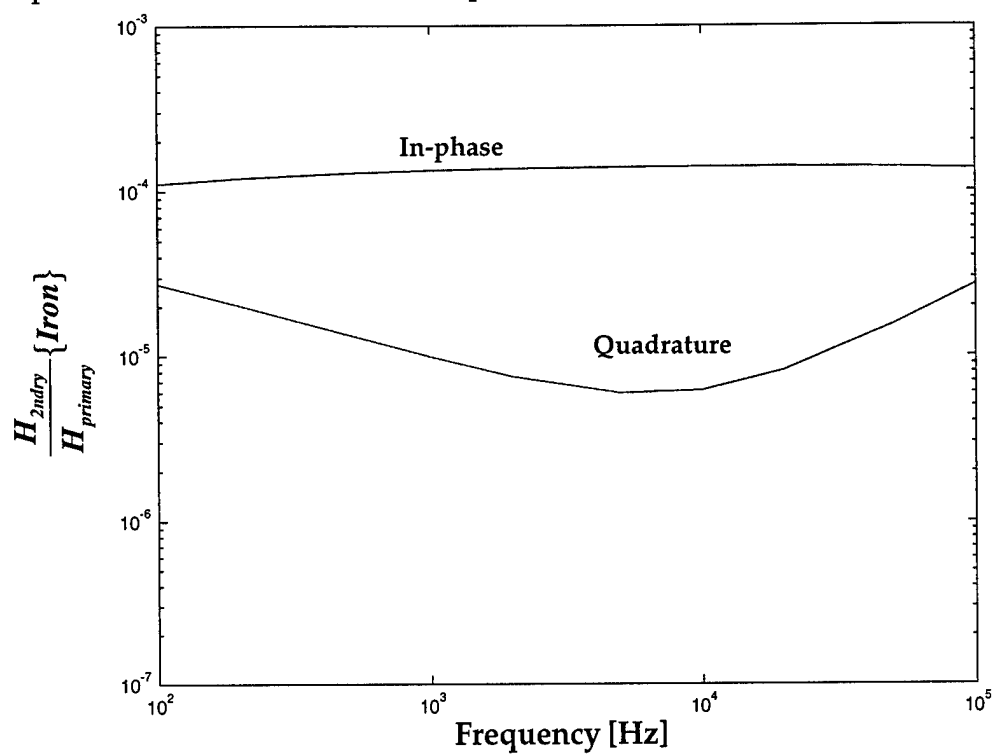


Figure 21: Plot of the secondary to primary z-axis H-field ratio at the "receive" point due to the induced z-axis VMD for the configuration given in Figure 19 with an iron sphere (high permeability).

Sensor Response Modeling

The sensor system to be evaluated by the tools developed during this effort is the GEM-2 from Geophex, Ltd of Raleigh, North Carolina. We have contacted Geophex and they have supplied us with information on their sensor systems, including the GEM-2. There are a number of key issues that need to be addressed prior to any sensor system evaluation; these are listed below along with relevant information for the GEM-2.

Issues Relating to the Sensor Evaluation

Type/nature of the source	VMD (coil parallel to earth surface)
Type/nature of the sensor	Coil (coplanar with source coil)
Source and sensor orientations	Both are coplanar and parallel to the earth surface
Source and sensor height above ground	Both 1 meter above the earth surface
Source and sensor lateral distance from the underground structure	Variable - see results below
Frequency band of operation	100 Hz - 22 kHz
Ground properties and layers/homogeneity of the earth	Two layer earth (see Figure 22, below for material properties)
Underground structure size, shape, location, and material properties	A 1 meter radius sphere made of either aluminum or iron. Depth at: 2m, 4m, 6m
External noise	Taken from Figure 12 of this Report using a 0.2 second measurement period (5 Hz)
Sensor internal noise	Assumed negligible for this analysis
Sensitivity of the sensor system	100 PPM of field strength

GEM-2: System Evaluation

We give a brief description of the GEM-2 here with the overall system properties; a more complete description can be found in various publications given in the references (Won, et al, 1996; Keiswetter and Won, 1997; Won and Keiswetter, 1997). These publications detail the specific "bucking coil" technique used to cancel (or "buck") the primary field (direct signal from the source coil) from the receiver

coil; this nulling is good to about 1 part in 10,000 or 100 PPM (parts-per-million) of the field strength. From an overall system point of view the GEM-2 can be viewed as a board a few inches wide and about 1.8 meters in length with coplanar coils at either end, the centers of these coils being separated by 1.66 meters. One coil acts as

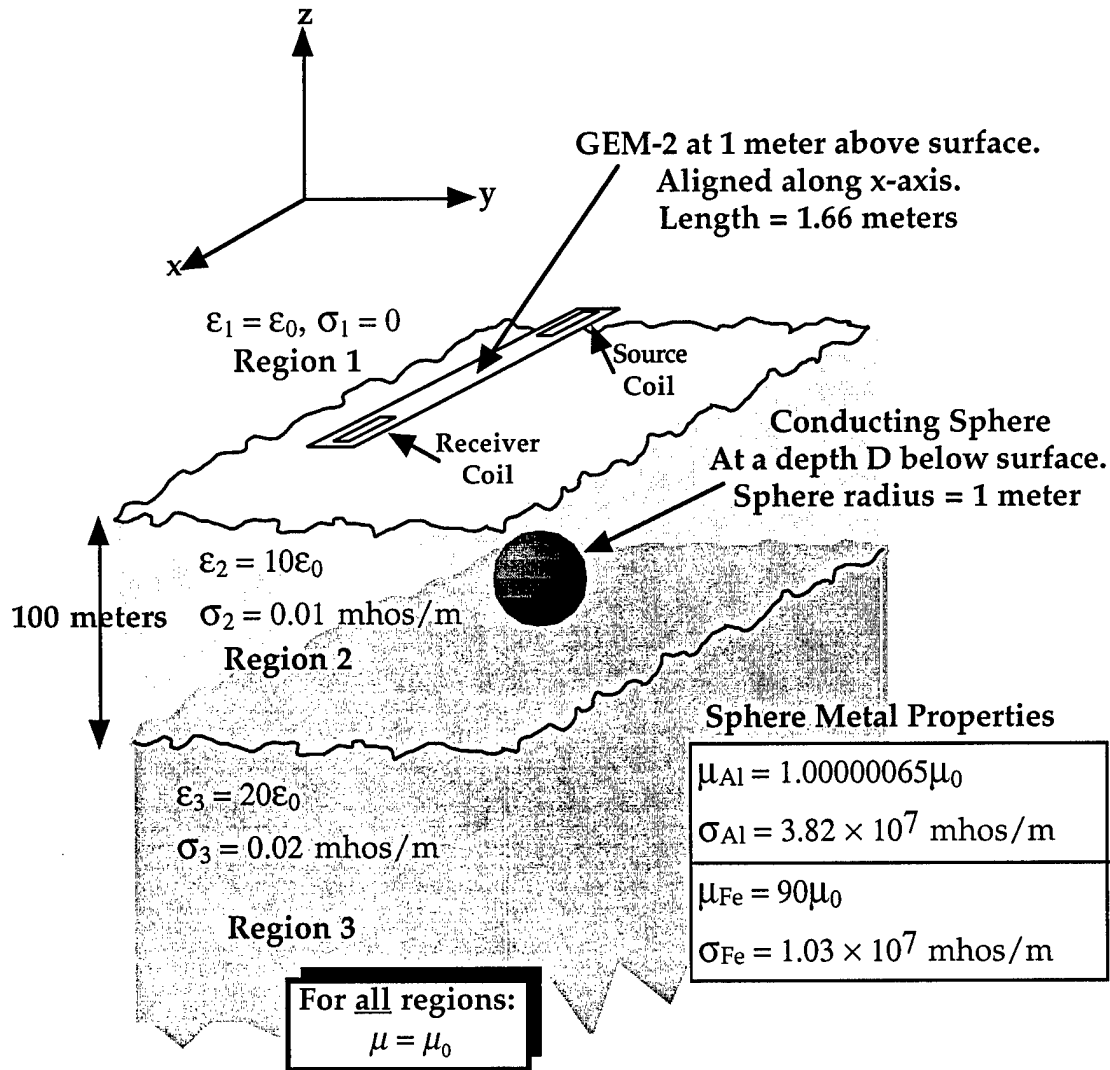


Figure 22: Sketch of GEM-2 sensor evaluation configuration
the source magnetic dipole, the other acts as a receiver. The source coil has an effective magnetic moment of 3 amp-m² (consistent with the GEM-2). The board may be held so that the plane containing the coils is parallel or perpendicular to the earth. The parallel configuration is called the horizontal coplanar configuration and corresponds to a VMD configuration; the perpendicular configuration is called the vertical coplanar configuration and corresponds to an HMD configuration. In our

evaluation here we will examine the horizontal coplanar (VMD) configuration. The GEM-2 can generate multiple frequencies over a period of about 0.2 seconds; this permits a wide variety of waveforms to be radiated. Calculations are made by moving this GEM-2 sensor pair over a region above a conducting sphere. The line determined by the sensor pair is parallel to the x-axis (see Figure 22). We examine a number of configurations: varying frequency, target depth, and material properties. In all cases we plot in-phase (real) and quadrature (imaginary) values for the ratio of the secondary H_z field to the primary H_z field at the receiver. The calculations will include the complete effective induced magnetic dipole on the sphere: both the induced VMD, the induced x-axis HMD, and the induced y-axis HMD. We will give the results as 3-D color plots showing the secondary H_z field to the primary H_z field ratio at the receiver. The in-phase and quadrature are given separately. The plots in each Figure are at a given frequency (100 Hz, 1 kHz, 10 kHz); the variation within the Figure are the depth, D , of the sphere (2 m, 4 m, 6 m) and the sphere material (aluminum, iron). The color intensity is chosen to threshold at about 100 PPM, consistent with the sensitivity of the GEM-2. The effect of average external noise is negligible for this configuration at these frequencies of operation as seen below in the calculated noise values in PPM relative to the primary field (using Figure 12, 5 Hz BW, and $H_{\text{Primary}} \approx 0.05 \text{ Amp/m}$).

<u>Frequency</u>	<u>Noise Value Ratio</u>
100 Hz	1.08 PPM
1 kHz	0.068 PPM
10 kHz	0.0043 PPM

Figures 23-25 examine the in-phase results and Figures 26-28 show the quadrature results.

The variation of the in-phase signal as the depth is increased is dramatic: at 2 meters the signal is "off the charts", at 4 meters the signal is quite detectable but greatly reduced, and at 6 meters the signal is below the threshold. The frequency variation of the in-phase signal is slight - the only noticeable effect is the slight increase in the iron sphere signal at 1 kHz and 10 kHz over the 100 Hz signal.

For all but the 2 meter depth iron sphere the quadrature results are below threshold. At 100 Hz this signal is well above threshold and it drops to a marginal value at 10 kHz for the quadrature signal.

100 Hz, In-phase

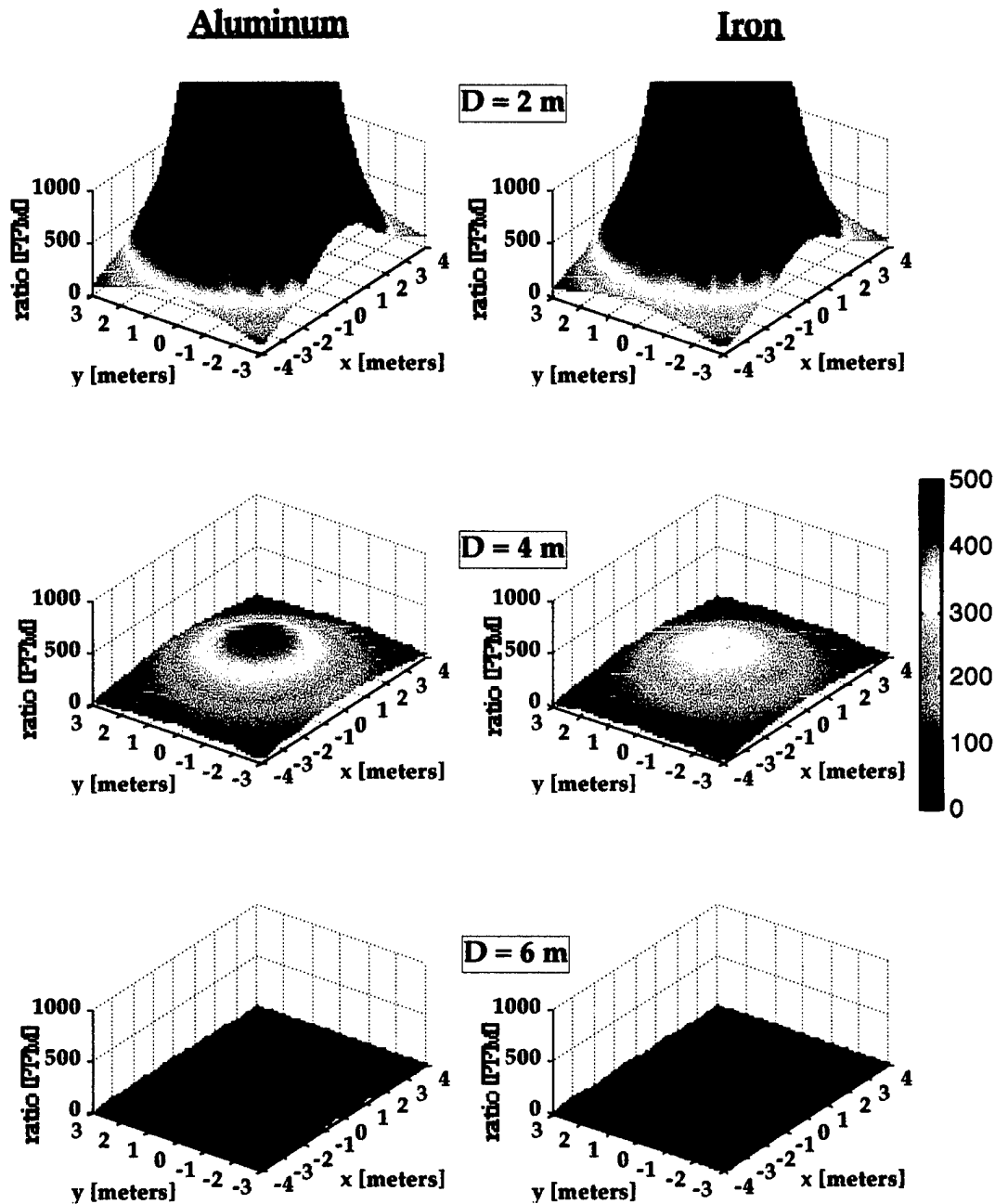


Figure 23: Plots of in-phase secondary to primary field ratio for GEM-2 sensor evaluation configuration given in Figure 22 for an aluminum sphere (left) and an iron sphere (right) at 100 Hz. Depth of sphere, D , varies from 2 to 6 meters.

1 kHz, In-phase

Aluminum

Iron

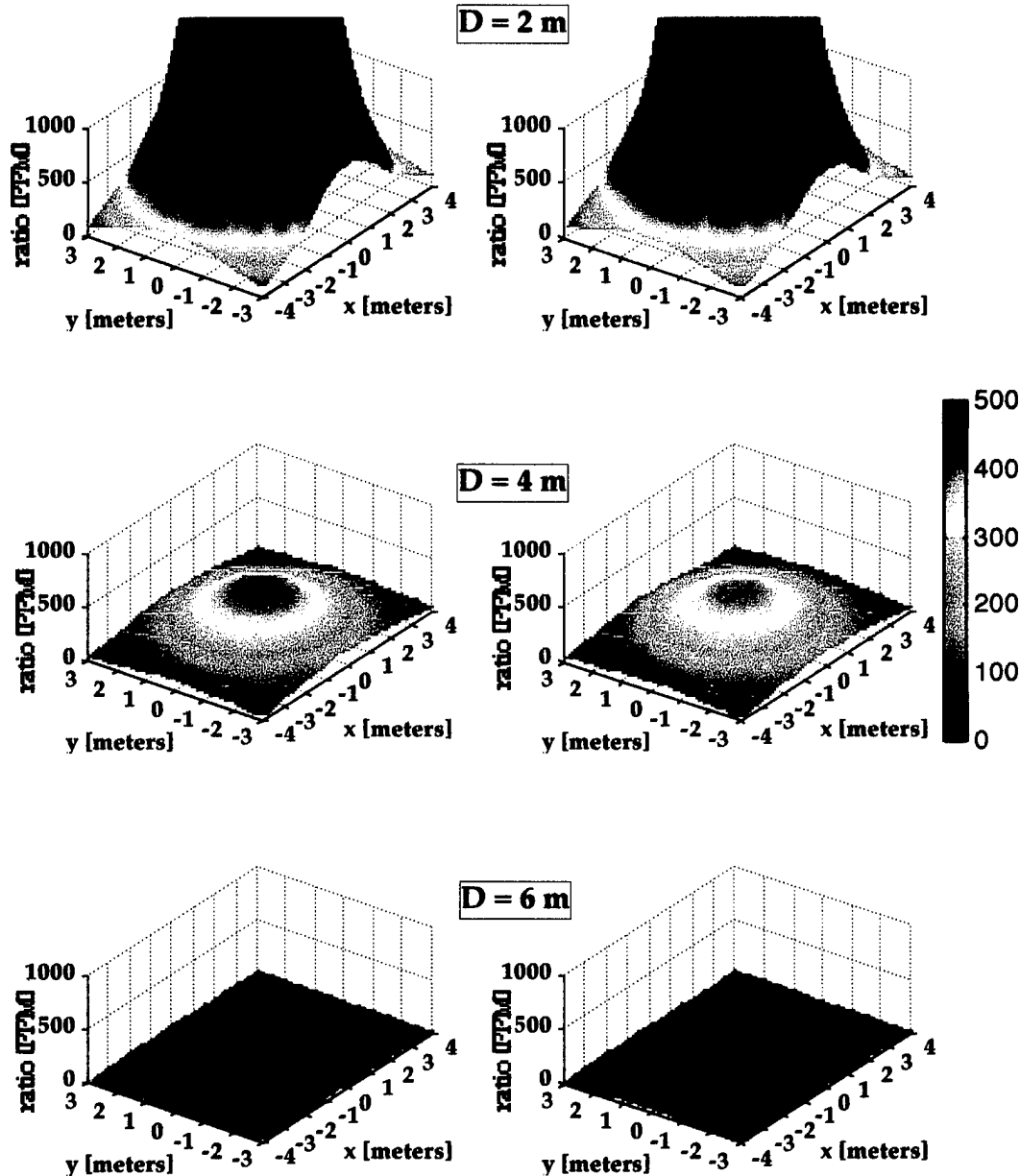


Figure 24: Plots of in-phase secondary to primary field ratio for GEM-2 sensor evaluation configuration for an aluminum sphere (left) and an iron sphere (right) at 1 kHz. Depth of sphere, D , varies from 2 to 6 meters.

10 kHz, In-phase

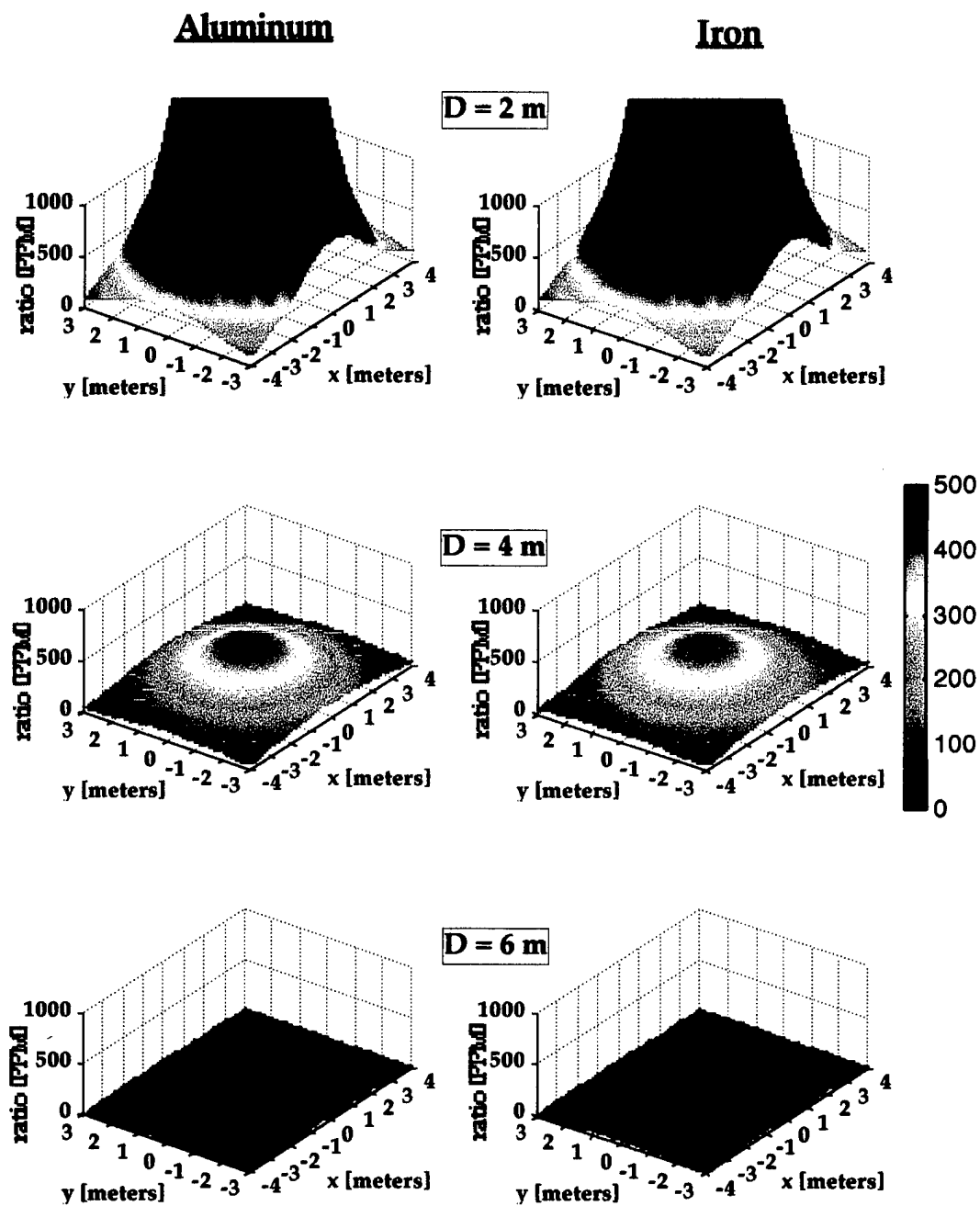


Figure 25: Plots of in-phase secondary to primary field ratio for GEM-2 sensor evaluation configuration for an aluminum sphere (left) and an iron sphere (right) at 10 kHz. Depth of sphere, D , varies from 2 to 6 meters.

100 Hz, Quadrature

Aluminum

Iron

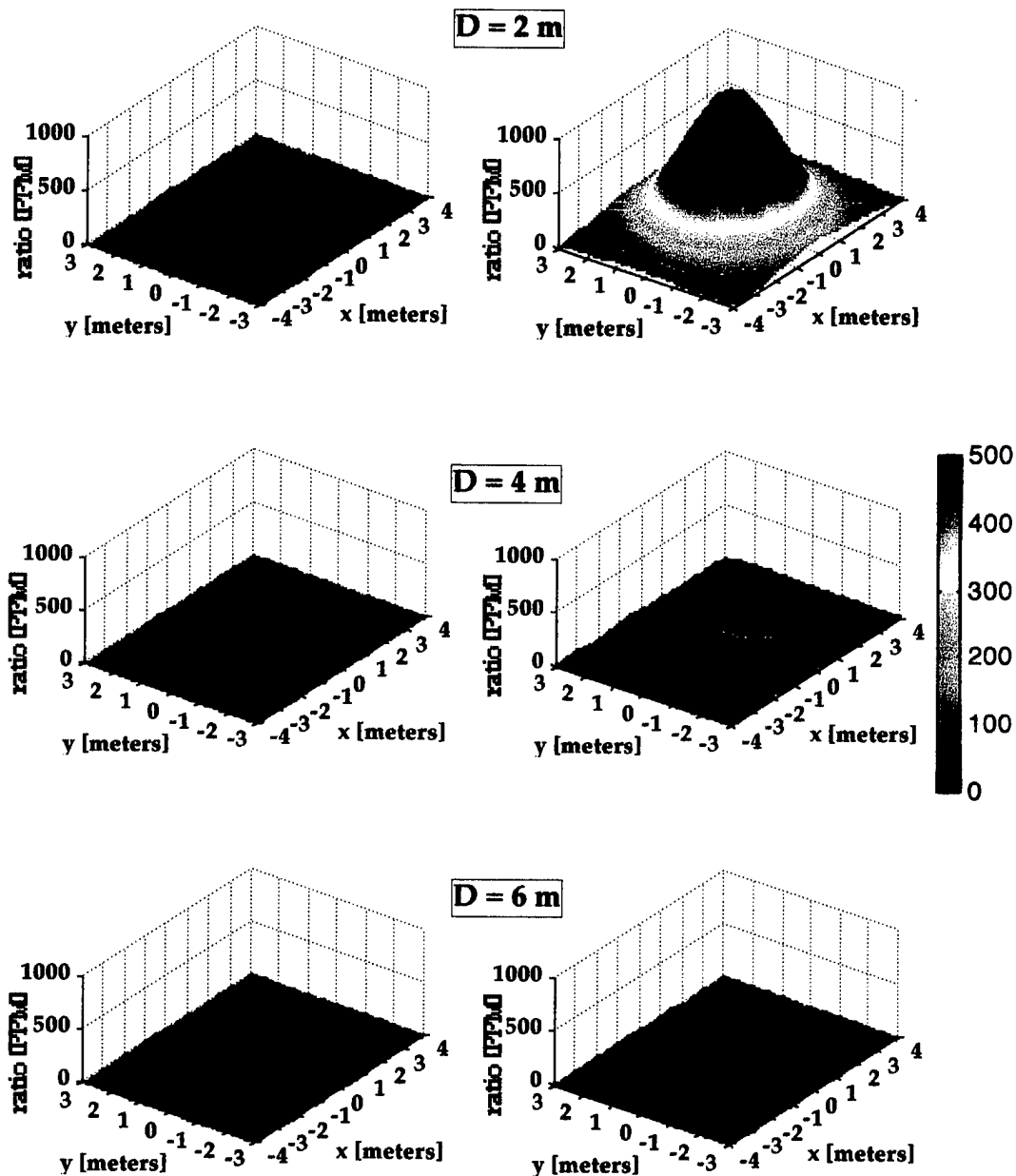


Figure 26: Plots of quadrature secondary to primary field ratio for GEM-2 sensor evaluation configuration for an aluminum sphere (left) and an iron sphere (right) at 100 Hz. Depth of sphere, D , varies from 2 to 6 meters.

1 kHz, Quadrature

Aluminum

Iron

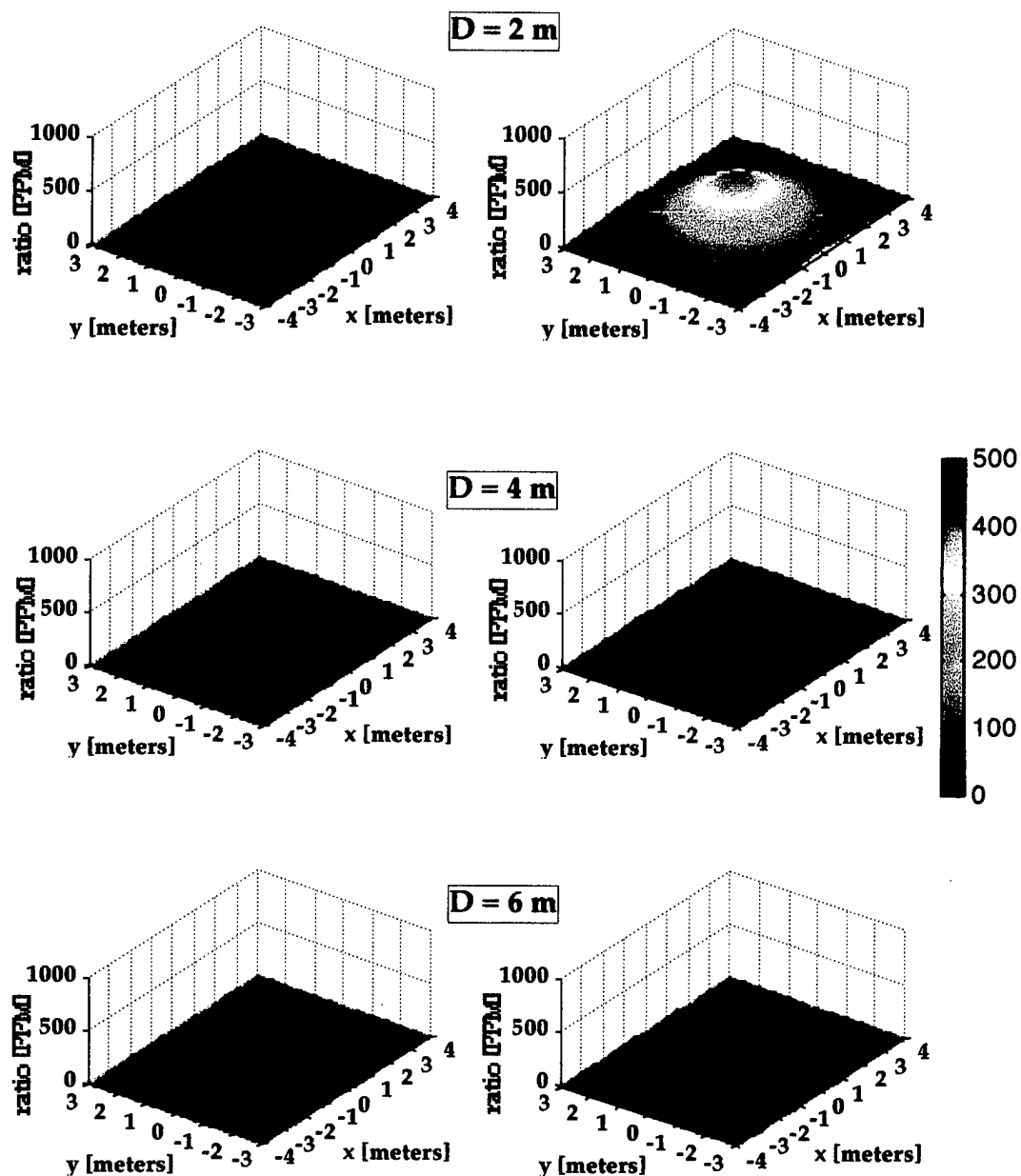


Figure 27: Plots of quadrature secondary to primary field ratio for GEM-2 sensor evaluation configuration for an aluminum sphere (left) and an iron sphere (right) at 1 kHz. Depth of sphere, D , varies from 2 to 6 meters.

10 kHz, Quadrature

Aluminum

Iron

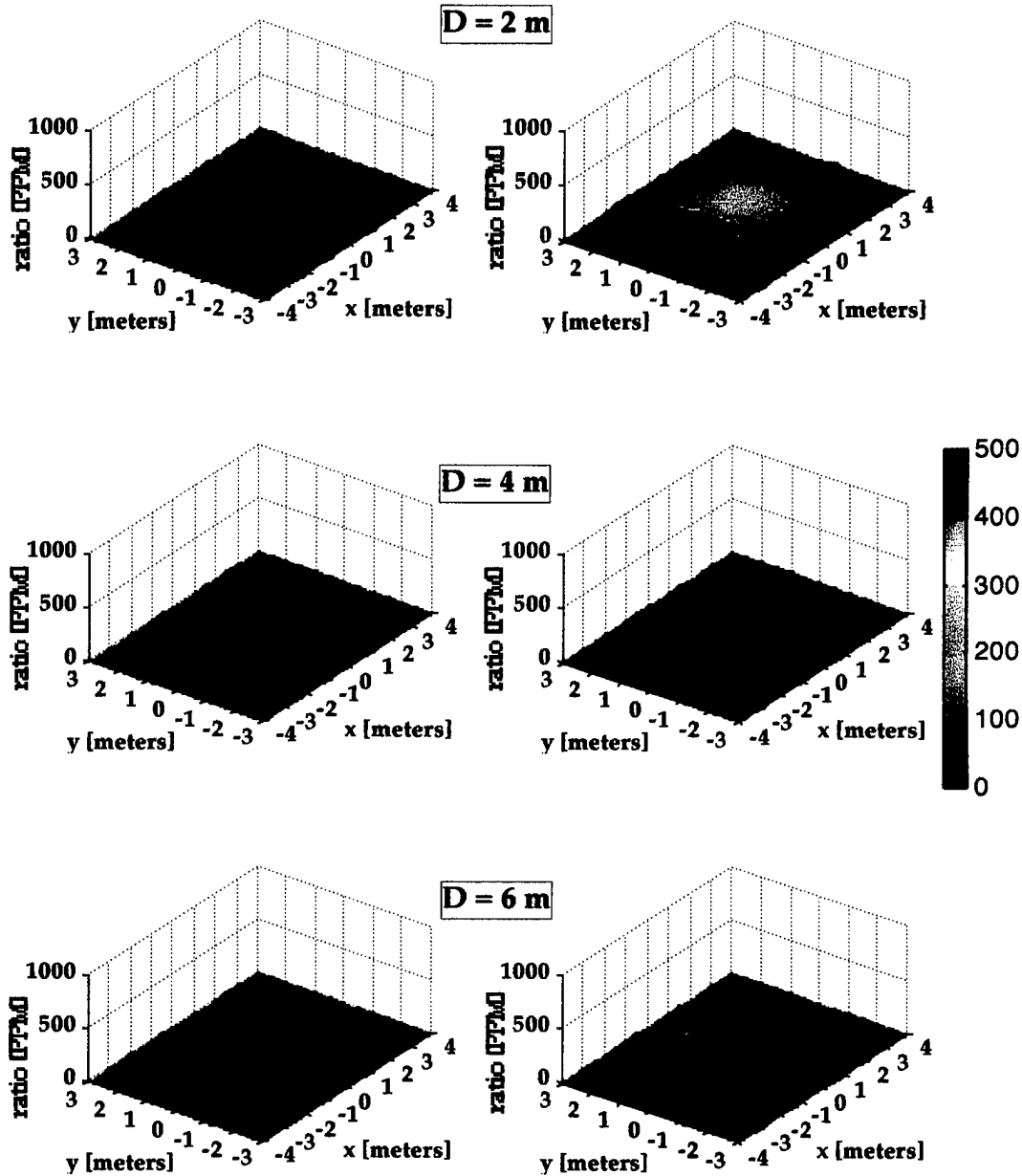


Figure 28: Plots of quadrature secondary to primary field ratio for GEM-2 sensor evaluation configuration for an aluminum sphere (left) and an iron sphere (right) at 10 kHz. Depth of sphere, D , varies from 2 to 6 meters.

Suggested Phase II Tasks

Below we list some suggested tasks for a Phase II effort that would be consistent with further enhancing and validating the tools developed during Phase I.

- **Remote Man-Made Source System Evaluation and Validation**

Identify a sensor system that could be used with HAARP/HIPAS and evaluate it using the MATLAB tools; test it in coordination with HAARP/HIPAS facilities.

- **Local Man-Made Source System Evaluation, Optimization, and Validation**

Using the MATLAB tools, demonstrate techniques for optimizing a given sensor system. Extend the system evaluation of the GEM-2 to other structures, e.g. pipes. Perform a system evaluation on the GEM-3 from Geophex. Validate the results from these evaluations and optimization using controlled experiments. Examine the feasibility and sensitivity of Geophex-derived sensors for aircraft surveillance.

References

- Barrick, D.E., Exact ULF/ELF Dipole Field Strengths in an Ideal Earth/Ionosphere Cavity over the Schumann Resonance Region, (to be published in *Radio Science*, 1998)
- Budden, K.G., *The Propagation of Radio Waves: The Theory of Radio Waves of Low Power in the Ionosphere and Magnetosphere*, Cambridge University Press, 669 pages, 1985 (corrected paperback edition 1988)
- Chew, C.C., *Waves and Fields in Inhomogeneous Media*, IEEE Press Series on Electromagnetic Waves, 608 pages, 1995
- Davies, K., *Ionospheric Radio Waves*, Blaisdell Publishing Company (a Division of Ginn and Company), 460 pages, 1969
- Fraser-Smith, A.C., P.R. McGill, A. Bernardi, R.A. Heliwell, and M.E. Ladd (1991), Global measurements of low-frequency radio noise, Chapter 5.1 in *Environmental and Space Electromagnetics*, H. Kikuchi, Ed, Springer-Verlag: New York, pp. 191-200.
- Keiswetter, D.A. and Won, I.J., Multifrequency Electromagnetic Signature of the Cloud Chamber, Nevada Test Site, *Journal of Environmental & Engineering Geophysics*, Vol. 2, Issue 2, 99-103, September 1997
- Lanzerotti, L.J., C.G. MacLennan, and A.C. Fraser-Smith (1990), Background magnetic spectra: $\sim 10^{-5}$ to $\sim 10^5$ Hz, *Geophys. Res. Letters*, Vol. 17, 1593-1596.
- Wait, J.R., A conducting sphere in a time varying magnetic field, *Geophysics*, 16, No. 4, 666-672, October 1951
- Wait, J.R., Electromagnetic Induction in a Small Conducting Sphere Above a Resistive Half Space, *Radio Science*, Vol. 3 (New Series), No. 10, 1030-1034 October 1968
- Wait, J.R., *Electromagnetic Waves in Stratified Media*, IEEE Press, 372 pages, 1996
- Won, I.J., Keiswetter, D.A., Fields, G.R.A., Sutton, L.C. GEM-2: A New Multifrequency Electromagnetic Sensor, *Journal of Environmental & Engineering Geophysics*, Vol. 1, Issue 2, 129-137, August 1996
- Won, I.J. and Keiswetter, D.A., Comparison of Magnetic and Electromagnetic Anomalies Caused by Underground Structures, *Journal of Environmental & Engineering Geophysics*, Vol. 2, Issue 2, 115-125, September 1997

Appendix A

Definitions:

$$\begin{aligned}
k_{nz} &= \sqrt{k_n^2 - k_p^2}, & k_n &= \omega \sqrt{\epsilon_n \mu_n} \\
T_{12}^{TM} &= \frac{2\epsilon_2 k_{1z}}{\epsilon_2 k_{1z} + \epsilon_1 k_{2z}}, & T_{21}^{TM} &= \frac{2\epsilon_1 k_{2z}}{\epsilon_2 k_{1z} + \epsilon_1 k_{2z}}, & T_{21}^{TE} &= \frac{2\mu_1 k_{2z}}{\mu_2 k_{1z} + \mu_1 k_{2z}} \\
R_{12}^{TM} &= \frac{\epsilon_2 k_{1z} - \epsilon_1 k_{2z}}{\epsilon_2 k_{1z} + \epsilon_1 k_{2z}}, & R_{21}^{TM} &= -R_{12}^{TM}, & R_{21}^{TE} &= -R_{12}^{TE} \\
T_{23}^{TM} &= \frac{2\epsilon_3 k_{2z}}{\epsilon_3 k_{2z} + \epsilon_2 k_{3z}}, & T_{23}^{TE} &= \frac{2\mu_3 k_{2z}}{\mu_3 k_{2z} + \mu_2 k_{3z}}, & R_{23}^{TE} &= \frac{\mu_3 k_{2z} - \mu_2 k_{3z}}{\mu_3 k_{2z} + \mu_2 k_{3z}} \\
\tilde{R}_{12}^{TM} &= \frac{R_{12}^{TM} + \tilde{R}_{23}^{TM} e^{2ik_{2z}(d_2-d_1)}}{1 + R_{12}^{TM} \tilde{R}_{23}^{TM} e^{2ik_{2z}(d_2-d_1)}}, & \tilde{R}_{12}^{TE} &= \frac{R_{12}^{TE} + \tilde{R}_{23}^{TE} e^{2ik_{2z}(d_2-d_1)}}{1 + R_{12}^{TE} \tilde{R}_{23}^{TE} e^{2ik_{2z}(d_2-d_1)}} \\
\tilde{R}_{21}^{TM} &= R_{21}^{TM}, & \tilde{R}_{23}^{TM} &= R_{23}^{TM}, & \tilde{R}_{23}^{TE} &= R_{23}^{TE} \\
\tilde{T}_{21}^{TM} &= T_{21}^{TM} = \frac{\epsilon_1 k_{2z}}{\epsilon_2 k_{1z}} T_{12}^{TM}, & \tilde{T}_{21}^{TE} &= T_{21}^{TE} = \frac{\mu_1 k_{2z}}{\mu_2 k_{1z}} T_{12}^{TE} \\
A_2^{TM} &= \frac{T_{12}^{TM} e^{i(k_{1z}-k_{2z})d_1}}{1 + R_{12}^{TM} \tilde{R}_{23}^{TM} e^{2ik_{2z}(d_2-d_1)}}, & A_2^{TE} &= \frac{T_{12}^{TE} e^{i(k_{1z}-k_{2z})d_1}}{1 + R_{12}^{TE} \tilde{R}_{23}^{TE} e^{2ik_{2z}(d_2-d_1)}} \\
B_2^{TM} &= \frac{e^{ik_{2z}z_0} - R_{23}^{TM} e^{ik_{2z}(2d_2-z_0)}}{1 + R_{12}^{TM} R_{23}^{TM} e^{2ik_{2z}(d_2-d_1)}}, & B_2^{TE} &= \frac{e^{ik_{2z}z_0} + e^{ik_{2z}(2d_2-z_0)} R_{23}^{TE}}{1 + R_{12}^{TE} \tilde{R}_{23}^{TE} e^{2ik_{2z}(d_2-d_1)}} \\
C_2^{TM} &= \frac{-e^{-ik_{2z}z_0} + e^{-ik_{2z}(2d_1-z_0)} R_{21}^{TM}}{1 + R_{12}^{TM} \tilde{R}_{23}^{TM} e^{2ik_{2z}(d_2-d_1)}}, & C_2^{TE} &= \frac{e^{-ik_{2z}z_0} + e^{-ik_{2z}(2d_1-z_0)} R_{21}^{TE}}{1 + R_{12}^{TE} \tilde{R}_{23}^{TE} e^{2ik_{2z}(d_2-d_1)}} \\
M_2^{TM} &= \frac{e^{ik_{2z}z_0} + R_{23}^{TM} e^{ik_{2z}(2d_2-z_0)}}{1 + R_{12}^{TM} R_{23}^{TM} e^{2ik_{2z}(d_2-d_1)}}, & M_2^{TE} &= \frac{e^{ik_{2z}z_0} - e^{ik_{2z}(2d_2-z_0)} R_{23}^{TE}}{1 + R_{12}^{TE} \tilde{R}_{23}^{TE} e^{2ik_{2z}(d_2-d_1)}} \\
N_2^{TM} &= \frac{e^{-ik_{2z}z_0} + e^{-ik_{2z}(2d_1-z_0)} R_{21}^{TM}}{1 + R_{12}^{TM} \tilde{R}_{23}^{TM} e^{2ik_{2z}(d_2-d_1)}}, & N_2^{TE} &= \frac{-e^{-ik_{2z}z_0} + e^{-ik_{2z}(2d_1-z_0)} R_{21}^{TE}}{1 + R_{12}^{TE} \tilde{R}_{23}^{TE} e^{2ik_{2z}(d_2-d_1)}}
\end{aligned}$$

VED in Region 1

Located at $z = 0$ - Interface 1-2 at $z = -d_1$ - Interface 2-3 at $z = -d_2$

Fields in Region 1: ($z \geq -d_1$)

$$E_{1\phi}^{VED[1]} = 0, \quad H_{1\rho}^{VED[1]} = 0, \quad H_{1z}^{VED[1]} = 0$$

$$E_{1z}^{VED[1]} = -\frac{Il}{4\pi\omega\epsilon_1} \int_0^\infty dk_\rho \frac{k_\rho^3}{k_{1z}} J_0(k_\rho \rho) \left[e^{ik_{1z}|z|} + \tilde{R}_{12}^{TM} e^{ik_{1z}(z+2d_1)} \right]$$

$$E_{1\rho}^{VED[1]} = i \frac{Il}{4\pi\omega\epsilon_1} \begin{cases} \int_0^\infty dk_\rho k_\rho^2 J_1(k_\rho \rho) \left[e^{ik_{1z}|z|} + \tilde{R}_{12}^{TM} e^{ik_{1z}(z+2d_1)} \right] & z \geq 0 \\ \int_0^\infty dk_\rho k_\rho^2 J_1(k_\rho \rho) \left[-e^{ik_{1z}|z|} + \tilde{R}_{12}^{TM} e^{ik_{1z}(z+2d_1)} \right] & -d_1 \leq z < 0 \end{cases}$$

$$H_{1\phi}^{VED[1]} = i \frac{Il}{4\pi} \int_0^\infty dk_\rho \frac{k_\rho^2}{k_{1z}} J_1(k_\rho \rho) \left[e^{ik_{1z}|z|} + \tilde{R}_{12}^{TM} e^{ik_{1z}(z+2d_1)} \right]$$

Fields in Region 2: ($-d_1 > z \geq -d_2$)

$$E_{2\phi}^{VED[1]} = 0, \quad H_{2\rho}^{VED[1]} = 0, \quad H_{2z}^{VED[1]} = 0$$

$$E_{2z}^{VED[1]} = -\frac{Il}{4\pi\omega\epsilon_2} \int_0^\infty dk_\rho \frac{k_\rho^3}{k_{1z}} J_0(k_\rho \rho) A_2^{TM} \left[e^{-ik_{2z}z} + \tilde{R}_{23}^{TM} e^{ik_{2z}(z+2d_2)} \right]$$

$$E_{2\rho}^{VED[1]} = i \frac{Il}{4\pi\omega\epsilon_2} \int_0^\infty dk_\rho \frac{k_{2z} k_\rho^2}{k_{1z}} J_1(k_\rho \rho) A_2^{TM} \left[-e^{-ik_{2z}z} + \tilde{R}_{23}^{TM} e^{ik_{2z}(z+2d_2)} \right]$$

$$H_{2\phi}^{VED[1]} = i \frac{Il}{4\pi} \int_0^\infty dk_\rho \frac{k_\rho^2}{k_{1z}} J_1(k_\rho \rho) A_2^{TM} \left[e^{-ik_{2z}z} + \tilde{R}_{23}^{TM} e^{ik_{2z}(z+2d_2)} \right]$$

VMD in Region 1

Located at $z = 0$ - Interface 1-2 at $z = -d_1$ - Interface 2-3 at $z = -d_2$

Fields in Region 1: ($z \geq -d_1$)

$$E_{1z}^{VMD[1]} = 0, \quad E_{1\rho}^{VMD[1]} = 0, \quad H_{1\phi}^{VMD[1]} = 0$$

$$E_{1\phi}^{VMD[1]} = \frac{\omega\mu_1 IA}{4\pi} \int_0^\infty dk_\rho \frac{k_\rho^2}{k_{1z}} J_1(k_\rho \rho) \left[e^{ik_{1z}|z|} + \tilde{R}_{12}^{TE} e^{ik_{1z}(z+2d_1)} \right]$$

$$H_{1z}^{VMD[1]} = -i \frac{IA}{4\pi} \int_0^\infty dk_\rho \frac{k_\rho^3}{k_{1z}} J_0(k_\rho \rho) \left[e^{ik_{1z}|z|} + \tilde{R}_{12}^{TE} e^{ik_{1z}(z+2d_1)} \right]$$

$$H_{1\rho}^{VMD[1]} = -\frac{IA}{4\pi} \left\{ \int_0^\infty dk_\rho k_\rho^2 J_1(k_\rho \rho) \left[e^{ik_{1z}|z|} + \tilde{R}_{12}^{TE} e^{ik_{1z}(z+2d_1)} \right] \right. \\ \left. \int_0^\infty dk_\rho k_\rho^2 J_1(k_\rho \rho) \left[-e^{ik_{1z}|z|} + \tilde{R}_{12}^{TE} e^{ik_{1z}(z+2d_1)} \right] \right\} \quad \begin{matrix} z \geq 0 \\ -d_1 \leq z < 0 \end{matrix}$$

Fields in Region 2: ($-d_1 > z \geq -d_2$)

$$E_{2z}^{VMD[1]} = 0, \quad E_{2\rho}^{VMD[1]} = 0, \quad H_{2\phi}^{VMD[1]} = 0$$

$$E_{2\phi}^{VMD[1]} = \omega\mu_1 \frac{IA}{4\pi} \int_0^\infty dk_\rho \frac{k_\rho^2}{k_{1z}} J_1(k_\rho \rho) A_2^{TE} \left[e^{-ik_{2z}z} + \tilde{R}_{23}^{TE} e^{ik_{2z}(z+2d_2)} \right]$$

$$H_{2z}^{VMD[1]} = -i \frac{IA\mu_1}{4\pi\mu_2} \int_0^\infty dk_\rho \frac{k_\rho^3}{k_{1z}} J_0(k_\rho \rho) A_2^{TE} \left[e^{-ik_{2z}z} + \tilde{R}_{23}^{TE} e^{ik_{2z}(z+2d_2)} \right]$$

$$H_{2\rho}^{VMD[1]} = -\frac{IA\mu_1}{4\pi\mu_2} \int_0^\infty dk_\rho \frac{k_{2z} k_\rho^2}{k_{1z}} J_1(k_\rho \rho) A_2^{TE} \left[-e^{-ik_{2z}z} + \tilde{R}_{23}^{TE} e^{ik_{2z}(z+2d_2)} \right]$$

VED in Region 2

Located at $z = -z_0$ ($-d_2 \leq -z_0 < -d_1$) - Interface 1-2 at $z = -d_1$ - Interface 2-3 at $z = -d_2$

Fields in Region 1: ($z \geq -d_1$)

$$E_{1\phi}^{VED[2]} = 0, \quad H_{1\rho}^{VED[2]} = 0, \quad H_{1z}^{VED[2]} = 0$$

$$E_{1z}^{VED[2]} = -\frac{Il}{4\pi\omega\epsilon_1} \int_0^\infty dk_\rho \frac{k_\rho^3}{k_{2z}} J_0(k_\rho) e^{ik_{1z}(z+d_1)} e^{-ik_{2z}d_1} \tilde{T}_{21}^{TM} B_2^{TM}$$

$$E_{1\rho}^{VED[2]} = i \frac{Il}{4\pi\omega\epsilon_1} \int_0^\infty dk_\rho \frac{k_{1z} k_\rho^2}{k_{2z}} J_1(k_\rho) e^{ik_{1z}(z+d_1)} e^{-ik_{2z}d_1} \tilde{T}_{21}^{TM} B_2^{TM}$$

$$H_{1\phi}^{VED[2]} = i \frac{Il}{4\pi} \int_0^\infty dk_\rho \frac{k_\rho^2}{k_{2z}} J_1(k_\rho) e^{ik_{1z}(z+d_1)} e^{-ik_{2z}d_1} \tilde{T}_{21}^{TM} B_2^{TM}$$

Fields in Region 2 above the source: ($-d_1 > z \geq -z_0$)

$$E_{2\phi}^{VED[2]} = 0, \quad H_{2\rho}^{VED[2]} = 0, \quad H_{2z}^{VED[2]} = 0$$

$$E_{2z}^{VED[2]} = -\frac{Il}{4\pi\omega\epsilon_2} \int_0^\infty dk_\rho \frac{k_\rho^3}{k_{2z}} J_0(k_\rho) B_2^{TM} \left(e^{ik_{2z}z} + e^{-ik_{2z}(z+2d_1)} R_{21}^{TM} \right)$$

$$E_{2\rho}^{VED[2]} = i \frac{Il}{4\pi\omega\epsilon_2} \int_0^\infty dk_\rho k_\rho^2 J_1(k_\rho) B_2^{TM} \left(e^{ik_{2z}z} - e^{-ik_{2z}(z+2d_1)} R_{21}^{TM} \right)$$

$$H_{2\phi}^{VED[2]} = i \frac{Il}{4\pi} \int_0^\infty dk_\rho \frac{k_\rho^2}{k_{2z}} J_1(k_\rho) B_2^{TM} \left(e^{ik_{2z}z} + e^{-ik_{2z}(z+2d_1)} R_{21}^{TM} \right)$$

VMD in Region 2

Located at $z = -z_0$ ($-d_2 \leq -z_0 < -d_1$) - Interface 1-2 at $z = -d_1$ - Interface 2-3 at $z = -d_2$

Fields in Region 1: ($z \geq -d_1$)

$$H_{1\phi}^{VMD[2]} = 0, \quad E_{1\rho}^{VMD[2]} = 0, \quad E_{1z}^{VMD[2]} = 0$$

$$H_{1z}^{VMD[2]} = -i \frac{IA\mu_2}{4\pi\mu_1} \int_0^\infty dk_\rho \frac{k_\rho^3}{k_{2z}} J_0(k_\rho \rho) e^{ik_{1z}(z+d_1)} e^{-ik_{2z}d_1} \tilde{T}_{21}^{TE} B_2^{TE}$$

$$H_{1\rho}^{VMD[2]} = -\frac{IA\mu_2}{4\pi\mu_1} \int_0^\infty dk_\rho \frac{k_\rho^2}{k_{2z}} J_1(k_\rho \rho) e^{ik_{1z}(z+d_1)} e^{-ik_{2z}d_1} \tilde{T}_{21}^{TE} B_2^{TE}$$

$$E_{1\phi}^{VMD[2]} = \omega\mu_2 \frac{IA}{4\pi} \int_0^\infty dk_\rho \frac{k_\rho^2}{k_{2z}} J_1(k_\rho \rho) e^{ik_{1z}(z+d_1)} e^{-ik_{2z}d_1} \tilde{T}_{21}^{TE} B_2^{TE}$$

Fields in Region 2 above the source: ($-d_1 > z \geq -z_0$)

$$H_{2\phi}^{VMD[2]} = 0, \quad E_{2\rho}^{VMD[2]} = 0, \quad E_{2z}^{VMD[2]} = 0$$

$$H_{2z}^{VMD[2]} = -i \frac{IA}{4\pi} \int_0^\infty dk_\rho \frac{k_\rho^3}{k_{2z}} J_0(k_\rho \rho) B_2^{TE} (e^{ik_{2z}z} + e^{-ik_{2z}(z+2d_1)} R_{21}^{TE})$$

$$H_{2\rho}^{VMD[2]} = -\frac{IA}{4\pi} \int_0^\infty dk_\rho k_\rho^2 J_1(k_\rho \rho) B_2^{TE} (e^{ik_{2z}z} - e^{-ik_{2z}(z+2d_1)} R_{21}^{TE})$$

$$E_{2\phi}^{VMD[2]} = \omega\mu_2 \frac{IA}{4\pi} \int_0^\infty dk_\rho \frac{k_\rho^2}{k_{2z}} J_1(k_\rho \rho) B_2^{TE} (e^{ik_{2z}z} + e^{-ik_{2z}(z+2d_1)} R_{21}^{TE})$$

HED in Region 1

Located at $z = 0$ - Interface 1-2 at $z = -d_1$ - Interface 2-3 at $z = -d_2$

Fields in Region 1: ($z \geq -d_1$)

$$E_{1z}^{HED[1]} = i \frac{Il}{4\pi\omega\epsilon_1} \cos\phi \left\{ \int_0^\infty dk_\rho k_\rho^2 J_1(k_\rho \rho) \left(e^{ik_{1z}|z|} - \tilde{R}_{12}^{TM} e^{ik_{1z}(z+2d_1)} \right) \right. \quad z \geq 0$$

$$\left. \int_0^\infty dk_\rho k_\rho^2 J_1(k_\rho \rho) \left(-e^{ik_{1z}|z|} - \tilde{R}_{12}^{TM} e^{ik_{1z}(z+2d_1)} \right) \right\} \quad z < 0$$

$$H_{1z}^{HED[1]} = i \frac{Il}{4\pi} \sin\phi \int_0^\infty dk_\rho \frac{k_\rho^2}{k_{1z}} J_1(k_\rho \rho) \left(e^{ik_{1z}|z|} + \tilde{R}_{12}^{TE} e^{ik_{1z}(z+2d_1)} \right)$$

$$E_{1\rho}^{HED[1]} = -\frac{Il}{4\pi\omega\epsilon_1} \cos\phi \int_0^\infty dk_\rho k_{1z} k_\rho \left(J_0(k_\rho \rho) - \frac{J_1(k_\rho \rho)}{k_\rho \rho} \right) \left(e^{ik_{1z}|z|} - \tilde{R}_{12}^{TM} e^{ik_{1z}(z+2d_1)} \right)$$

$$-k_1^2 \frac{Il}{4\pi\omega\epsilon_1 \rho} \cos\phi \int_0^\infty dk_\rho \frac{1}{k_{1z}} J_1(k_\rho \rho) \left(e^{ik_{1z}|z|} + \tilde{R}_{12}^{TE} e^{ik_{1z}(z+2d_1)} \right)$$

$$E_{1\phi}^{HED[1]} = -\frac{Il}{4\pi\omega\epsilon_1 \rho} \sin\phi \int_0^\infty dk_\rho k_{1z} J_1(k_\rho \rho) \left(e^{ik_{1z}|z|} - \tilde{R}_{12}^{TM} e^{ik_{1z}(z+2d_1)} \right)$$

$$+k_1^2 \frac{Il}{4\pi\omega\epsilon_1} \sin\phi \int_0^\infty dk_\rho \frac{1}{k_{1z}} k_\rho \left(J_0(k_\rho \rho) - \frac{J_1(k_\rho \rho)}{k_\rho \rho} \right) \left(e^{ik_{1z}|z|} + \tilde{R}_{12}^{TE} e^{ik_{1z}(z+2d_1)} \right)$$

$$\begin{aligned}
H_{1\rho}^{HED[1]} &= \frac{Il}{4\pi} \sin\phi \int_0^\infty dk_\rho k_\rho \left\{ \frac{J_1(k_\rho \rho)}{k_\rho \rho} (\tilde{R}_{12}^{TE} + \tilde{R}_{12}^{TM}) - J_0(k_\rho \rho) \tilde{R}_{12}^{TE} \right\} e^{ik_{1z}(z+2d_1)} \\
&\quad + \frac{Il}{4\pi} \sin\phi \left\{ \begin{aligned} &-\int_0^\infty dk_\rho k_\rho J_0(k_\rho \rho) e^{ik_{1z}|z|} & z \geq 0 \\ &\int_0^\infty dk_\rho k_\rho J_0(k_\rho \rho) e^{ik_{1z}|z|} & -d_1 \leq z < 0 \end{aligned} \right\} \\
H_{1\phi}^{HED[1]} &= \frac{Il}{4\pi} \cos\phi \int_0^\infty dk_\rho k_\rho \left\{ J_0(k_\rho \rho) \tilde{R}_{12}^{TM} - \frac{J_1(k_\rho \rho)}{k_\rho \rho} (\tilde{R}_{12}^{TM} + \tilde{R}_{12}^{TE}) \right\} e^{ik_{1z}(z+2d_1)} \\
&\quad + \frac{Il}{4\pi} \cos\phi \left\{ \begin{aligned} &-\int_0^\infty dk_\rho k_\rho J_0(k_\rho \rho) e^{ik_{1z}|z|} & z \geq 0 \\ &\int_0^\infty dk_\rho k_\rho J_0(k_\rho \rho) e^{ik_{1z}|z|} & -d_1 \leq z < 0 \end{aligned} \right\}
\end{aligned}$$

Fields in Region 2: $(-d_1 > z \geq -d_2)$

$$\begin{aligned}
E_{2z}^{HED[1]} &= -i \frac{Il}{4\pi\omega\epsilon_2} \cos\phi \int_0^\infty dk_\rho k_\rho^2 J_1(k_\rho \rho) A_2^{TM} \left(e^{-ik_{2z}z} + \tilde{R}_{23}^{TM} e^{ik_{2z}(z+2d_2)} \right) \\
H_{2z}^{HED[1]} &= i \frac{Il}{4\pi} \frac{\mu_1}{\mu_2} \sin\phi \int_0^\infty dk_\rho \frac{k_\rho^2}{k_{1z}} J_1(k_\rho \rho) A_2^{TE} \left(e^{-ik_{2z}z} + \tilde{R}_{23}^{TE} e^{ik_{2z}(z+2d_2)} \right)
\end{aligned}$$

$$E_{2\rho}^{HED[1]} = \frac{Il}{4\pi\omega\epsilon_2} \cos\phi \int_0^\infty dk_\rho A_2^{TM} k_{2z} k_\rho \left(J_0(k_\rho \rho) - \frac{J_1(k_\rho \rho)}{k_\rho \rho} \right) \left(-e^{-ik_{2z}z} + \tilde{R}_{23}^{TM} e^{ik_{2z}(z+2d_2)} \right)$$

$$-k_2^2 \frac{Il}{4\pi\rho\omega\epsilon_2} \frac{\mu_1}{\mu_2} \cos\phi \int_0^\infty dk_\rho A_2^{TE} \frac{1}{k_{1z}} J_1(k_\rho \rho) \left(e^{-ik_{2z}z} + \tilde{R}_{23}^{TE} e^{ik_{2z}(z+2d_2)} \right)$$

$$E_{2\phi}^{HED[1]} = \frac{Il}{4\pi\rho\omega\epsilon_2} \sin\phi \int_0^\infty dk_\rho A_2^{TM} k_{2z} J_1(k_\rho \rho) \left(-e^{-ik_{2z}z} + \tilde{R}_{23}^{TM} e^{ik_{2z}(z+2d_2)} \right) \\ + k_2^2 \frac{Il}{4\pi\omega\epsilon_2} \frac{\mu_1}{\mu_2} \sin\phi \int_0^\infty dk_\rho \frac{A_2^{TE} k_\rho}{k_{1z}} \left(J_0(k_\rho \rho) - \frac{J_1(k_\rho \rho)}{k_\rho \rho} \right) \left(e^{-ik_{2z}z} + \tilde{R}_{23}^{TE} e^{ik_{2z}(z+2d_2)} \right)$$

$$H_{2\rho}^{HED[1]} = \frac{Il}{4\pi\rho} \sin\phi \int_0^\infty dk_\rho A_2^{TM} J_1(k_\rho \rho) \left(e^{-ik_{2z}z} + \tilde{R}_{23}^{TM} e^{ik_{2z}(z+2d_2)} \right) \\ - \frac{Il}{4\pi} \frac{\mu_1}{\mu_2} \sin\phi \int_0^\infty dk_\rho \frac{A_2^{TE} k_{2z} k_\rho}{k_{1z}} \left(J_0(k_\rho \rho) - \frac{J_1(k_\rho \rho)}{k_\rho \rho} \right) \left(-e^{-ik_{2z}z} + \tilde{R}_{23}^{TE} e^{ik_{2z}(z+2d_2)} \right)$$

$$H_{2\phi}^{HED[1]} = \frac{Il}{4\pi} \cos\phi \int_0^\infty dk_\rho A_2^{TM} k_\rho \left(J_0(k_\rho \rho) - \frac{J_1(k_\rho \rho)}{k_\rho \rho} \right) \left(e^{-ik_{2z}z} + \tilde{R}_{23}^{TM} e^{ik_{2z}(z+2d_2)} \right) \\ - \frac{Il}{4\pi\rho} \frac{\mu_1}{\mu_2} \cos\phi \int_0^\infty dk_\rho \frac{A_2^{TE} k_{2z}}{k_{1z}} J_1(k_\rho \rho) \left(-e^{-ik_{2z}z} + \tilde{R}_{23}^{TE} e^{ik_{2z}(z+2d_2)} \right)$$

HMD in Region 1

Located at $z = 0$ - Interface 1-2 at $z = -d_1$ - Interface 2-3 at $z = -d_2$

Fields in Region 1: ($z \geq -d_1$)

$$H_{1z}^{HMD[1]} = -\frac{IA}{4\pi} \cos\phi \begin{cases} \int_0^\infty dk_\rho k_\rho^2 J_1(k_\rho \rho) (e^{ik_{1z}|z|} - \tilde{R}_{12}^{TE} e^{ik_{1z}(z+2d_1)}) & z \geq 0 \\ \int_0^\infty dk_\rho k_\rho^2 J_1(k_\rho \rho) (-e^{ik_{1z}|z|} - \tilde{R}_{12}^{TE} e^{ik_{1z}(z+2d_1)}) & z < 0 \end{cases}$$

$$E_{1z}^{HMD[1]} = \frac{\omega\mu_1 IA}{4\pi} \sin\phi \int_0^\infty dk_\rho \frac{k_\rho^2}{k_{1z}} J_1(k_\rho \rho) (e^{ik_{1z}|z|} + \tilde{R}_{12}^{TM} e^{ik_{1z}(z+2d_1)})$$

$$H_{1\rho}^{HMD[1]} = -i \frac{IA}{4\pi} \cos\phi \int_0^\infty dk_\rho k_{1z} k_\rho \left(J_0(k_\rho \rho) - \frac{J_1(k_\rho \rho)}{k_\rho \rho} \right) (e^{ik_{1z}|z|} - \tilde{R}_{12}^{TE} e^{ik_{1z}(z+2d_1)})$$

$$-ik_1^2 \frac{IA}{4\pi\rho} \cos\phi \int_0^\infty dk_\rho \frac{1}{k_{1z}} J_1(k_\rho \rho) (e^{ik_{1z}|z|} + \tilde{R}_{12}^{TM} e^{ik_{1z}(z+2d_1)})$$

$$H_{1\phi}^{HMD[1]} = -i \frac{IA}{4\pi\rho} \sin\phi \int_0^\infty dk_\rho k_{1z} J_1(k_\rho \rho) (e^{ik_{1z}|z|} - \tilde{R}_{12}^{TE} e^{ik_{1z}(z+2d_1)})$$

$$+ik_1^2 \frac{IA}{4\pi} \sin\phi \int_0^\infty dk_\rho \frac{1}{k_{1z}} k_\rho \left(J_0(k_\rho \rho) - \frac{J_1(k_\rho \rho)}{k_\rho \rho} \right) (e^{ik_{1z}|z|} + \tilde{R}_{12}^{TM} e^{ik_{1z}(z+2d_1)})$$

$$\begin{aligned}
E_{1\rho}^{HMD[1]} &= -i \frac{\omega \mu_1 I A}{4\pi} \sin \phi \int_0^\infty dk_\rho k_\rho \left\{ \frac{J_1(k_\rho \rho)}{k_\rho \rho} (\tilde{R}_{12}^{TM} + \tilde{R}_{12}^{TE}) - J_0(k_\rho \rho) \tilde{R}_{12}^{TM} \right\} e^{ik_{1z}(z+2d_1)} \\
&\quad -i \frac{\omega \mu_1 I A}{4\pi} \sin \phi \left\{ \begin{aligned} &-\int_0^\infty dk_\rho k_\rho J_0(k_\rho \rho) e^{ik_{1z}|z|} & z \geq 0 \\ &\int_0^\infty dk_\rho k_\rho J_0(k_\rho \rho) e^{ik_{1z}|z|} & -d_1 \leq z < 0 \end{aligned} \right\} \\
E_{1\phi}^{HMD[1]} &= -i \frac{\omega \mu_1 I A}{4\pi} \cos \phi \int_0^\infty dk_\rho k_\rho \left(J_0(k_\rho \rho) \tilde{R}_{12}^{TE} - \frac{J_1(k_\rho \rho)}{k_\rho \rho} (\tilde{R}_{12}^{TE} + \tilde{R}_{12}^{TM}) \right) e^{ik_{1z}(z+2d_1)} \\
&\quad -i \frac{\omega \mu_1 I A}{4\pi} \cos \phi \left\{ \begin{aligned} &-\int_0^\infty dk_\rho k_\rho J_0(k_\rho \rho) e^{ik_{1z}|z|} & z \geq 0 \\ &\int_0^\infty dk_\rho k_\rho J_0(k_\rho \rho) e^{ik_{1z}|z|} & -d_1 \leq z < 0 \end{aligned} \right\}
\end{aligned}$$

Fields in Region 2: $(-d_1 > z \geq -d_2)$

$$\begin{aligned}
H_{2z}^{HMD[1]} &= \frac{\mu_1 I A}{4\pi \mu_2} \cos \phi \int_0^\infty dk_\rho k_\rho^2 J_1(k_\rho \rho) A_2^{TE} \left(e^{-ik_{2z}z} + \tilde{R}_{23}^{TE} e^{ik_{2z}(z+2d_2)} \right) \\
E_{2z}^{HMD[1]} &= \frac{\omega \mu_1 I A}{4\pi} \frac{\epsilon_1}{\epsilon_2} \sin \phi \int_0^\infty dk_\rho \frac{k_\rho^2}{k_{1z}} J_1(k_\rho \rho) A_2^{TM} \left(e^{-ik_{2z}z} + \tilde{R}_{23}^{TM} e^{ik_{2z}(z+2d_2)} \right)
\end{aligned}$$

$$H_{2\rho}^{HMD[1]} = i \frac{\mu_1 IA}{4\pi\mu_2} \cos\phi \int_0^\infty dk_\rho A_2^{TE} k_{2z} k_\rho \left(J_0(k_\rho \rho) - \frac{J_1(k_\rho \rho)}{k_\rho \rho} \right) \left(-e^{-ik_{2z}z} + \tilde{R}_{23}^{TE} e^{ik_{2z}(z+2d_2)} \right)$$

$$-ik_2^2 \frac{\mu_1 IA}{4\pi\rho\mu_2} \frac{\varepsilon_1}{\varepsilon_2} \cos\phi \int_0^\infty dk_\rho A_2^{TM} \frac{1}{k_{1z}} J_1(k_\rho \rho) \left(e^{-ik_{2z}z} + \tilde{R}_{23}^{TM} e^{ik_{2z}(z+2d_2)} \right)$$

$$H_{2\phi}^{HMD[1]} = i \frac{\mu_1 IA}{4\pi\rho\mu_2} \sin\phi \int_0^\infty dk_\rho A_2^{TE} k_{2z} J_1(k_\rho \rho) \left(-e^{-ik_{2z}z} + \tilde{R}_{23}^{TE} e^{ik_{2z}(z+2d_2)} \right) \\ + ik_2^2 \frac{\mu_1 IA}{4\pi\mu_2} \frac{\varepsilon_1}{\varepsilon_2} \sin\phi \int_0^\infty dk_\rho \frac{A_2^{TM} k_\rho}{k_{1z}} \left(J_0(k_\rho \rho) - \frac{J_1(k_\rho \rho)}{k_\rho \rho} \right) \left(e^{-ik_{2z}z} + \tilde{R}_{23}^{TM} e^{ik_{2z}(z+2d_2)} \right)$$

$$E_{2\rho}^{HMD[1]} = -i \frac{\omega\mu_1 IA}{4\pi\rho} \sin\phi \int_0^\infty dk_\rho A_2^{TE} J_1(k_\rho \rho) \left(e^{-ik_{2z}z} + \tilde{R}_{23}^{TE} e^{ik_{2z}(z+2d_2)} \right) \\ + i \frac{\omega\mu_1 IA}{4\pi} \frac{\varepsilon_1}{\varepsilon_2} \sin\phi \int_0^\infty dk_\rho \frac{A_2^{TM} k_{2z} k_\rho}{k_{1z}} \left(J_0(k_\rho \rho) - \frac{J_1(k_\rho \rho)}{k_\rho \rho} \right) \left(-e^{-ik_{2z}z} + \tilde{R}_{23}^{TM} e^{ik_{2z}(z+2d_2)} \right)$$

$$E_{2\phi}^{HMD[1]} = -i \frac{\omega\mu_1 IA}{4\pi} \cos\phi \int_0^\infty dk_\rho A_2^{TE} k_\rho \left(J_0(k_\rho \rho) - \frac{J_1(k_\rho \rho)}{k_\rho \rho} \right) \left(e^{-ik_{2z}z} + \tilde{R}_{23}^{TE} e^{ik_{2z}(z+2d_2)} \right) \\ + i \frac{\omega\mu_1 IA}{4\pi\rho} \frac{\varepsilon_1}{\varepsilon_2} \cos\phi \int_0^\infty dk_\rho \frac{A_2^{TM} k_{2z}}{k_{1z}} J_1(k_\rho \rho) \left(-e^{-ik_{2z}z} + \tilde{R}_{23}^{TM} e^{ik_{2z}(z+2d_2)} \right)$$

HED in Region 2

Located at $z = -z_0$ - Interface 1-2 at $z = -d_1$ - Interface 2-3 at $z = -d_2$

Fields in Region 1: ($z \geq -d_1$)

$$E_{1z}^{HED[2]} = i \frac{Il}{4\pi\omega\epsilon_1} \cos\phi \int_0^\infty dk_\rho k_\rho^2 J_1(k_\rho \rho) e^{ik_{1z}(z+d_1)} e^{-ik_{2z}d_1} \tilde{T}_{21}^{TM} B_2^{TM}$$

$$H_{1z}^{HED[2]} = i \frac{Il}{4\pi} \frac{\mu_2}{\mu_1} \sin\phi \int_0^\infty dk_\rho \frac{k_\rho^2}{k_{2z}} J_1(k_\rho \rho) e^{ik_{1z}(z+d_1)} e^{-ik_{2z}d_1} \tilde{T}_{21}^{TE} B_2^{TE}$$

$$E_{1\rho}^{HED[2]} = -\frac{Il}{4\pi\omega\epsilon_1} \cos\phi \int_0^\infty dk_\rho k_{1z} k_\rho \left(J_0(k_\rho \rho) - \frac{J_1(k_\rho \rho)}{k_\rho \rho} \right) e^{ik_{1z}(z+d_1)} e^{-ik_{2z}d_1} \tilde{T}_{21}^{TM} B_2^{TM}$$

$$-k_1^2 \frac{Il}{4\pi\omega\epsilon_1 \rho} \mu_1 \cos\phi \int_0^\infty dk_\rho \frac{1}{k_{2z}} J_1(k_\rho \rho) e^{ik_{1z}(z+d_1)} e^{-ik_{2z}d_1} \tilde{T}_{21}^{TE} B_2^{TE}$$

$$E_{1\phi}^{HED[2]} = \frac{Il}{4\pi\omega\epsilon_1 \rho} \sin\phi \int_0^\infty dk_\rho k_{1z} J_1(k_\rho \rho) e^{ik_{1z}(z+d_1)} e^{-ik_{2z}d_1} \tilde{T}_{21}^{TM} B_2^{TM}$$

$$+k_1^2 \frac{Il}{4\pi\omega\epsilon_1} \frac{\mu_2}{\mu_1} \sin\phi \int_0^\infty dk_\rho \frac{1}{k_{2z}} k_\rho \left(J_0(k_\rho \rho) - \frac{J_1(k_\rho \rho)}{k_\rho \rho} \right) e^{ik_{1z}(z+d_1)} e^{-ik_{2z}d_1} \tilde{T}_{21}^{TE} B_2^{TE}$$

$$H_{1\rho}^{HED[2]} = -\frac{Il}{4\pi\rho} \sin\phi \int_0^\infty dk_\rho J_1(k_\rho \rho) e^{ik_{1z}(z+d_1)} e^{-ik_{2z}d_1} \tilde{T}_{21}^{TM} B_2^{TM}$$

$$-\frac{Il}{4\pi} \frac{\mu_2}{\mu_1} \sin\phi \int_0^\infty dk_\rho \frac{k_{1z}}{k_{2z}} k_\rho \left(J_0(k_\rho \rho) - \frac{J_1(k_\rho \rho)}{k_\rho \rho} \right) e^{ik_{1z}(z+d_1)} e^{-ik_{2z}d_1} \tilde{T}_{21}^{TE} B_2^{TE}$$

$$H_{1\phi}^{HED[2]} = -\frac{Il}{4\pi} \cos\phi \int_0^\infty dk_\rho k_\rho \left(J_0(k_\rho \rho) - \frac{J_1(k_\rho \rho)}{k_\rho \rho} \right) e^{ik_{1z}(z+d_1)} e^{-ik_{2z}d_1} \tilde{T}_{21}^{TM} B_2^{TM} \\ - \frac{Il}{4\pi\rho} \frac{\mu_2}{\mu_1} \cos\phi \int_0^\infty dk_\rho \frac{k_{1z}}{k_\rho} J_1(k_\rho \rho) e^{ik_{1z}(z+d_1)} e^{-ik_{2z}d_1} \tilde{T}_{21}^{TE} B_2^{TE}$$

Fields in Region 2 above the source: $(-d_1 > z \geq -z_0)$

$$E_{2z}^{HED[2]} = i \frac{Il}{4\pi\omega\epsilon_2} \cos\phi \int_0^\infty dk_\rho k_\rho^2 J_1(k_\rho \rho) B_2^{TM} (e^{ik_{2z}z} + e^{-ik_{2z}(z+2d_1)}) R_{21}^{TM} \\ H_{2z}^{HED[2]} = i \frac{Il}{4\pi} \sin\phi \int_0^\infty dk_\rho \frac{k_\rho^2}{k_{2z}} J_1(k_\rho \rho) B_2^{TE} (e^{ik_{2z}z} + e^{-ik_{2z}(z+2d_1)}) R_{21}^{TE} \\ E_{2\rho}^{HED[2]} = -\frac{Il}{4\pi\omega\epsilon_2} \cos\phi \int_0^\infty dk_\rho k_{2z} B_2^{TM} k_\rho \left(J_0(k_\rho \rho) - \frac{J_1(k_\rho \rho)}{k_\rho \rho} \right) (e^{ik_{2z}z} - e^{-ik_{2z}(z+2d_1)}) R_{21}^{TM} \\ - k_2^2 \frac{Il}{4\pi\omega\epsilon_2\rho} \cos\phi \int_0^\infty dk_\rho \frac{B_2^{TE}}{k_{2z}} J_1(k_\rho \rho) (e^{ik_{2z}z} + e^{-ik_{2z}(z+2d_1)}) R_{21}^{TE} \\ E_{2\phi}^{HED[2]} = \frac{Il}{4\pi\omega\epsilon_2\rho} \sin\phi \int_0^\infty dk_\rho k_{2z} B_2^{TM} J_1(k_\rho \rho) (e^{ik_{2z}z} - e^{-ik_{2z}(z+2d_1)}) R_{21}^{TM} \\ + k_2^2 \frac{Il}{4\pi\omega\epsilon_2} \sin\phi \int_0^\infty dk_\rho \frac{k_\rho B_2^{TE}}{k_{2z}} \left(J_0(k_\rho \rho) - \frac{J_1(k_\rho \rho)}{k_\rho \rho} \right) (e^{ik_{2z}z} + e^{-ik_{2z}(z+2d_1)}) R_{21}^{TE}$$

$$\begin{aligned}
H_{2\rho}^{HED[2]} &= -\frac{Il}{4\pi\rho} \sin\phi \int_0^\infty dk_\rho B_2^{TM} J_1(k_\rho\rho) \left(e^{ik_{2z}z} + e^{-ik_{2z}(z+2d_1)} R_{21}^{TM} \right) \\
&\quad - \frac{Il}{4\pi} \sin\phi \int_0^\infty dk_\rho B_2^{TE} k_\rho \left(J_0(k_\rho\rho) - \frac{J_1(k_\rho\rho)}{k_\rho\rho} \right) \left(e^{ik_{2z}z} - e^{-ik_{2z}(z+2d_1)} R_{21}^{TE} \right) \\
H_{2\phi}^{HED[2]} &= -\frac{Il}{4\pi} \cos\phi \int_0^\infty dk_\rho B_2^{TM} k_\rho \left(J_0(k_\rho\rho) - \frac{J_1(k_\rho\rho)}{k_\rho\rho} \right) \left(e^{ik_{2z}z} + e^{-ik_{2z}(z+2d_1)} R_{21}^{TM} \right) \\
&\quad - \frac{Il}{4\pi\rho} \cos\phi \int_0^\infty dk_\rho B_2^{TE} J_1(k_\rho\rho) \left(e^{ik_{2z}z} - e^{-ik_{2z}(z+2d_1)} R_{21}^{TE} \right)
\end{aligned}$$

Fields in Region 2 below the source: $(-z_0 \geq z > -d_2)$

$$\begin{aligned}
E_{2z}^{HED[2]} &= i \frac{Il}{4\pi\omega\epsilon_2} \cos\phi \int_0^\infty dk_\rho k_\rho^2 J_1(k_\rho\rho) C_2^{TM} \left(e^{-ik_{2z}z} + e^{ik_{2z}(z+2d_2)} R_{23}^{TM} \right) \\
H_{2z}^{HED[2]} &= i \frac{Il}{4\pi} \sin\phi \int_0^\infty dk_\rho \frac{k_\rho^2}{k_{2z}} J_1(k_\rho\rho) C_2^{TE} \left(e^{-ik_{2z}z} + e^{ik_{2z}(z+2d_2)} R_{23}^{TE} \right) \\
E_{2\rho}^{HED[2]} &= -\frac{Il}{4\pi\omega\epsilon_2} \cos\phi \int_0^\infty dk_\rho k_{2z} k_\rho \left(J_0(k_\rho\rho) - \frac{J_1(k_\rho\rho)}{k_\rho\rho} \right) C_2^{TM} \left(-e^{-ik_{2z}z} + e^{ik_{2z}(z+2d_2)} R_{23}^{TM} \right) \\
&\quad - k_2^2 \frac{Il}{4\pi\omega\epsilon_2\rho} \cos\phi \int_0^\infty dk_\rho \frac{1}{k_{2z}} J_1(k_\rho\rho) C_2^{TE} \left(e^{-ik_{2z}z} + e^{ik_{2z}(z+2d_2)} R_{23}^{TE} \right)
\end{aligned}$$

$$\begin{aligned}
E_{2\phi}^{HED[2]} &= \frac{Il}{4\pi\omega\varepsilon_2\rho} \sin\phi \int_0^\infty dk_\rho k_{2z} J_1(k_\rho\rho) C_2^{TM} \left(-e^{-ik_{2z}z} + e^{ik_{2z}(z+2d_2)} R_{23}^{TM} \right) \\
&\quad + k_2^2 \frac{Il}{4\pi\omega\varepsilon_2} \sin\phi \int_0^\infty dk_\rho \frac{k_\rho}{k_{2z}} \left(J_0(k_\rho\rho) - \frac{J_1(k_\rho\rho)}{k_\rho\rho} \right) C_2^{TE} \left(e^{-ik_{2z}z} + e^{ik_{2z}(z+2d_2)} R_{23}^{TE} \right) \\
H_{2\rho}^{HED[2]} &= -\frac{Il}{4\pi\rho} \sin\phi \int_0^\infty dk_\rho J_1(k_\rho\rho) C_2^{TM} \left(e^{-ik_{2z}z} + e^{ik_{2z}(z+2d_2)} R_{23}^{TM} \right) \\
&\quad - \frac{Il}{4\pi} \sin\phi \int_0^\infty dk_\rho k_\rho \left(J_0(k_\rho\rho) - \frac{J_1(k_\rho\rho)}{k_\rho\rho} \right) C_2^{TE} \left(-e^{-ik_{2z}z} + e^{ik_{2z}(z+2d_2)} R_{23}^{TE} \right) \\
H_{2\phi}^{HED[2]} &= -\frac{Il}{4\pi} \cos\phi \int_0^\infty dk_\rho k_\rho \left(J_0(k_\rho\rho) - \frac{J_1(k_\rho\rho)}{k_\rho\rho} \right) C_2^{TM} \left(e^{-ik_{2z}z} + e^{ik_{2z}(z+2d_2)} R_{23}^{TM} \right) \\
&\quad - \frac{Il}{4\pi\rho} \cos\phi \int_0^\infty dk_\rho J_1(k_\rho\rho) C_2^{TE} \left(-e^{-ik_{2z}z} + e^{ik_{2z}(z+2d_2)} R_{23}^{TE} \right)
\end{aligned}$$

HMD in Region 2

Located at $z = -z_0$ - Interface 1-2 at $z = -d_1$ - Interface 2-3 at $z = -d_2$

Fields in Region 1: ($z \geq -d_1$)

$$E_{1z}^{HMD[2]} = \frac{\omega\mu_2 IA}{4\pi} \frac{\varepsilon_2}{\varepsilon_1} \sin\phi \int_0^\infty dk_\rho \frac{k_\rho^2}{k_{2z}} J_1(k_\rho \rho) e^{ik_{1z}(z+d_1)} e^{-ik_{2z}d_1} \tilde{T}_{21}^{TM} M_2^{TM}$$

$$H_{1z}^{HMD[2]} = -\frac{\mu_2 IA}{4\pi\mu_1} \cos\phi \int_0^\infty dk_\rho k_\rho^2 J_1(k_\rho \rho) e^{ik_{1z}(z+d_1)} e^{-ik_{2z}d_1} \tilde{T}_{21}^{TE} M_2^{TE}$$

$$E_{1\rho}^{HMD[2]} = \frac{i\omega\mu_2 IA}{4\pi\rho} \sin\phi \int_0^\infty dk_\rho J_1(k_\rho \rho) e^{ik_{1z}(z+d_1)} e^{-ik_{2z}d_1} \tilde{T}_{21}^{TE} M_2^{TE} \\ + \frac{i\omega\mu_2 IA}{4\pi} \frac{\varepsilon_2}{\varepsilon_1} \sin\phi \int_0^\infty dk_\rho \frac{k_{1z}}{k_{2z}} k_\rho \left(J_0(k_\rho \rho) - \frac{J_1(k_\rho \rho)}{k_\rho \rho} \right) e^{ik_{1z}(z+d_1)} e^{-ik_{2z}d_1} \tilde{T}_{21}^{TM} M_2^{TM}$$

$$E_{1\phi}^{HMD[2]} = \frac{i\omega\mu_2 IA}{4\pi} \cos\phi \int_0^\infty dk_\rho k_\rho \left(J_0(k_\rho \rho) - \frac{J_1(k_\rho \rho)}{k_\rho \rho} \right) e^{ik_{1z}(z+d_1)} e^{-ik_{2z}d_1} \tilde{T}_{21}^{TE} M_2^{TE}$$

$$+ \frac{i\omega\mu_2 IA}{4\pi\rho} \frac{\varepsilon_2}{\varepsilon_1} \cos\phi \int_0^\infty dk_\rho \frac{k_{1z}}{k_{2z}} J_1(k_\rho \rho) e^{ik_{1z}(z+d_1)} e^{-ik_{2z}d_1} \tilde{T}_{21}^{TM} M_2^{TM}$$

$$H_{1\rho}^{HMD[2]} = \frac{i\mu_2 IA}{4\pi\mu_1} \cos\phi \int_0^\infty dk_\rho k_{1z} k_\rho \left(J_0(k_\rho \rho) - \frac{J_1(k_\rho \rho)}{k_\rho \rho} \right) e^{ik_{1z}(z+d_1)} e^{-ik_{2z}d_1} \tilde{T}_{21}^{TE} M_2^{TE}$$

$$- k_1^2 \frac{i\mu_2 IA}{4\pi\mu_1 \rho} \frac{\varepsilon_2}{\varepsilon_1} \cos\phi \int_0^\infty dk_\rho \frac{1}{k_{2z}} J_1(k_\rho \rho) e^{ik_{1z}(z+d_1)} e^{-ik_{2z}d_1} \tilde{T}_{21}^{TM} M_2^{TM}$$

$$H_{1\phi}^{HMD[2]} = \frac{i\mu_2 IA}{4\pi\mu_1\rho} \sin\phi \int_0^\infty dk_\rho k_{1z} J_1(k_\rho\rho) e^{ik_{1z}(z+d_1)} e^{-ik_{2z}d_1} \tilde{T}_{21}^{TE} M_2^{TE} \\ + k_1^2 \frac{i\mu_2 IA}{4\pi\mu_1} \frac{\varepsilon_2}{\varepsilon_1} \sin\phi \int_0^\infty dk_\rho \frac{1}{k_{2z}} k_\rho \left(J_0(k_\rho\rho) - \frac{J_1(k_\rho\rho)}{k_\rho\rho} \right) e^{ik_{1z}(z+d_1)} e^{-ik_{2z}d_1} \tilde{T}_{21}^{TM} M_2^{TM}$$

Fields in Region 2 above the source: $(-d_1 > z \geq -z_0)$

$$E_{2z}^{HMD[2]} = \frac{\omega\mu_2 IA}{4\pi} \sin\phi \int_0^\infty dk_\rho \frac{k_\rho^2}{k_{2z}} J_1(k_\rho\rho) M_2^{TM} \left(e^{ik_{2z}z} + e^{-ik_{2z}(z+2d_1)} R_{21}^{TM} \right)$$

$$H_{2z}^{HMD[2]} = -\frac{IA}{4\pi} \cos\phi \int_0^\infty dk_\rho k_\rho^2 J_1(k_\rho\rho) M_2^{TE} \left(e^{ik_{2z}z} + e^{-ik_{2z}(z+2d_1)} R_{21}^{TE} \right)$$

$$E_{2\rho}^{HMD[2]} = \frac{i\omega\mu_2 IA}{4\pi\rho} \sin\phi \int_0^\infty dk_\rho M_2^{TE} J_1(k_\rho\rho) \left(e^{ik_{2z}z} + e^{-ik_{2z}(z+2d_1)} R_{21}^{TE} \right) \\ + \frac{i\omega\mu_2 IA}{4\pi} \sin\phi \int_0^\infty dk_\rho M_2^{TM} k_\rho \left(J_0(k_\rho\rho) - \frac{J_1(k_\rho\rho)}{k_\rho\rho} \right) \left(e^{ik_{2z}z} - e^{-ik_{2z}(z+2d_1)} R_{21}^{TM} \right)$$

$$E_{2\phi}^{HMD[2]} = \frac{i\omega\mu_2 IA}{4\pi} \cos\phi \int_0^\infty dk_\rho M_2^{TE} k_\rho \left(J_0(k_\rho\rho) - \frac{J_1(k_\rho\rho)}{k_\rho\rho} \right) \left(e^{ik_{2z}z} + e^{-ik_{2z}(z+2d_1)} R_{21}^{TE} \right) \\ + \frac{i\omega\mu_2 IA}{4\pi\rho} \cos\phi \int_0^\infty dk_\rho M_2^{TM} J_1(k_\rho\rho) \left(e^{ik_{2z}z} - e^{-ik_{2z}(z+2d_1)} R_{21}^{TM} \right)$$

$$\begin{aligned}
H_{2\rho}^{HMD[2]} &= -\frac{iIA}{4\pi} \cos\phi \int_0^\infty dk_\rho k_{2z} M_2^{TE} k_\rho \left(J_0(k_\rho \rho) - \frac{J_1(k_\rho \rho)}{k_\rho \rho} \right) \left(e^{ik_{2z}z} - e^{-ik_{2z}(z+2d_1)} R_{21}^{TE} \right) \\
&\quad - k_2^2 \frac{iIA}{4\pi\rho} \cos\phi \int_0^\infty dk_\rho \frac{M_2^{TM}}{k_{2z}} J_1(k_\rho \rho) \left(e^{ik_{2z}z} + e^{-ik_{2z}(z+2d_1)} R_{21}^{TM} \right) \\
H_{2\phi}^{HMD[2]} &= \frac{iIA}{4\pi\rho} \sin\phi \int_0^\infty dk_\rho k_{2z} M_2^{TE} J_1(k_\rho \rho) \left(e^{ik_{2z}z} - e^{-ik_{2z}(z+2d_1)} R_{21}^{TE} \right) \\
&\quad + k_2^2 \frac{iIA}{4\pi} \sin\phi \int_0^\infty dk_\rho \frac{k_\rho M_2^{TM}}{k_{2z}} \left(J_0(k_\rho \rho) - \frac{J_1(k_\rho \rho)}{k_\rho \rho} \right) \left(e^{ik_{2z}z} + e^{-ik_{2z}(z+2d_1)} R_{21}^{TM} \right)
\end{aligned}$$

Fields in Region 2 below the source: ($-z_0 \geq z > -d_2$)

$$\begin{aligned}
E_{2z}^{HMD[2]} &= \frac{\omega\mu_2 IA}{4\pi} \sin\phi \int_0^\infty dk_\rho \frac{k_\rho^2}{k_{2z}} J_1(k_\rho \rho) N_2^{TM} \left(e^{-ik_{2z}z} + e^{ik_{2z}(z+2d_2)} R_{23}^{TM} \right) \\
H_{2z}^{HMD[2]} &= -\frac{IA}{4\pi} \cos\phi \int_0^\infty dk_\rho k_\rho^2 J_1(k_\rho \rho) N_2^{TE} \left(e^{-ik_{2z}z} + e^{ik_{2z}(z+2d_2)} R_{23}^{TE} \right) \\
E_{2\rho}^{HMD[2]} &= \frac{i\omega\mu_2 IA}{4\pi\rho} \sin\phi \int_0^\infty dk_\rho J_1(k_\rho \rho) N_2^{TE} \left(e^{-ik_{2z}z} + e^{ik_{2z}(z+2d_2)} R_{23}^{TE} \right) \\
&\quad + \frac{i\omega\mu_2 IA}{4\pi} \sin\phi \int_0^\infty dk_\rho k_\rho \left(J_0(k_\rho \rho) - \frac{J_1(k_\rho \rho)}{k_\rho \rho} \right) N_2^{TM} \left(-e^{-ik_{2z}z} + e^{ik_{2z}(z+2d_2)} R_{23}^{TM} \right)
\end{aligned}$$

$$\begin{aligned}
E_{2\phi}^{HMD[2]} &= \frac{i\omega\mu_2 IA}{4\pi} \cos\phi \int_0^\infty dk_\rho k_\rho \left(J_0(k_\rho \rho) - \frac{J_1(k_\rho \rho)}{k_\rho \rho} \right) N_2^{TE} \left(e^{-ik_{2z}z} + e^{ik_{2z}(z+2d_2)} R_{23}^{TE} \right) \\
&\quad + \frac{i\omega\mu_2 IA}{4\pi\rho} \cos\phi \int_0^\infty dk_\rho J_1(k_\rho \rho) N_2^{TM} \left(-e^{-ik_{2z}z} + e^{ik_{2z}(z+2d_2)} R_{23}^{TM} \right) \\
H_{2\rho}^{HMD[2]} &= -\frac{iIA}{4\pi} \cos\phi \int_0^\infty dk_\rho k_{2z} k_\rho \left(J_0(k_\rho \rho) - \frac{J_1(k_\rho \rho)}{k_\rho \rho} \right) N_2^{TE} \left(-e^{-ik_{2z}z} + e^{ik_{2z}(z+2d_2)} R_{23}^{TE} \right) \\
&\quad - k_2^2 \frac{iIA}{4\pi\rho} \cos\phi \int_0^\infty dk_\rho \frac{1}{k_{2z}} J_1(k_\rho \rho) N_2^{TM} \left(e^{-ik_{2z}z} + e^{ik_{2z}(z+2d_2)} R_{23}^{TM} \right) \\
H_{2\phi}^{HMD[2]} &= \frac{iIA}{4\pi\rho} \sin\phi \int_0^\infty dk_\rho k_{2z} J_1(k_\rho \rho) N_2^{TE} \left(-e^{-ik_{2z}z} + e^{ik_{2z}(z+2d_2)} R_{23}^{TE} \right) \\
&\quad + k_2^2 \frac{iIA}{4\pi} \sin\phi \int_0^\infty dk_\rho \frac{k_\rho}{k_{2z}} \left(J_0(k_\rho \rho) - \frac{J_1(k_\rho \rho)}{k_\rho \rho} \right) N_2^{TM} \left(e^{-ik_{2z}z} + e^{ik_{2z}(z+2d_2)} R_{23}^{TM} \right)
\end{aligned}$$